Theoretical Study of the Nitric Oxide Dioxygenase Reaction of the Truncated Hemoglobin N from *Mycobacterium tuberculosis*

Lavinia Arielle Carabet

A Thesis
in
The Department of
Chemistry and Biochemistry

Presented in Partial Fulfillment of the Requirements
for the Degree of Master of Science (Chemistry option Biochemistry) at
Concordia University
Montreal, Quebec, Canada

August 2014

CONCORDIA UNIVERSITY
School of Graduate Studies

This is to certify that the thesis prepared

By: Lavinia Arielle Carabet

Entitled: Theoretical Study of the Nitric Oxide Dioxygenase Reaction of the Truncated Hemoglobin N from *Mycobacterium tuberculosis*

and submitted in partial fulfillment of the requirements for the degree of

Master of Science Chemistry option Biochemistry

complies with the regulations of the University and meets the accepted standards with respect to originality and quality.

Signed by the final examining committee:

Dr. Heidi Muchall Chair

Dr. Gilles Peslherbe Examiner

Dr. Ann English Examiner

Dr. Guillaume Lamoureux Supervisor

Approved by _____
Chair of Department or Graduate Program Director

_____
Dean of Faculty

Date August 20, 2014

ABSTRACT

Theoretical Study of the Nitric Oxide Dioxygenase Reaction of the Truncated Hemoglobin N from *Mycobacterium tuberculosis*

Lavinia Arielle Carabet

Tuberculosis (TB) is one of the oldest human afflictions and is still declared a major threat worldwide. The contemporary resurgence of the TB epidemic is due to multidrug-resistant strains of *Mycobacterium tuberculosis* (Mtb). The success of Mtb as a human lung pathogen is attributed to its capacity to survive in the alveolar macrophages of the host immune system by entering, for a prolonged time, a state of latency where it can resist oxidative and nitrosative species (e.g. O_2•$^-$ and •NO), and then reactivates to cause TB. •NO plays an important role in the host defense against the pathogen by inhibiting key biological processes. For instance, •NO and its highly reactive derivatives ($OONO^-$ and •NO_2) inhibit respiration and effect nitration that can lead to cell death. The truncated hemoglobin N (trHbN) of Mtb protects the aerobic respiration of the bacillus from •NO inhibition and prevents its own irreversible nitration, by actively metabolizing •NO to innocuous NO_3^-, through the rapid nitric oxide dioxygenase reaction (NOD). The NOD reaction is central to the defense system of Mtb, for coping with the toxic effects of •NO under hypoxia. The mechanism of the NOD reaction includes the formation of the $OONO^-$ intermediate and its isomerization to a nitrato-complex, followed by the release of the NO_3^- anion. Discrepancies exist in the literature with respect to the isomerization mechanism and the role of the active site residues in assisting the reaction. These aspects of the NOD reaction have been investigated here using state-of-the-art computational approaches. The results suggest a sequential mechanism with very short-lived intermediates. Distal Gln58, Tyr33, Leu54, Phe46, Phe32 and Val94 residues facilitate and cage the highly reactive $Fe^{IV}=O^{2-}$ and •NO_2 intermediates that result from $OONO^-$ homolysis. Tyr33 is involved in a dynamic H-bonding network with Gln58 and Leu54 backbone. Tyr33 changes conformations and transiently stabilizes the •NO_2 radical. Gln58 stabilizes the O-atom of oxo-ferryl species and assists •NO_2 rebinding via H-bonding. Phe46 stabilizes the bound product. The H-bonding network between Tyr33, Gln58 and Leu54 prevents the oxidation and nitration of Tyr33 by keeping the hydroxyl and phenyl groups at safe distance and orientation with respect to $Fe^{IV}=O^{2-}$ and •NO_2. Similar dynamics of the distal site residues have been observed for NO_3^- release. Tyr33, Gln58, Phe46 and Phe32 stabilize NO_3^- via H-bonding, and promote the breaking of the Fe^{III}-O bond of the bound NO_3^-, its dissociation and release.

Acknowledgements

I want to thank Dr. Guillaume Lamoureux for his supervision and for imparting his knowledge and rigorous scientific standards to his students. I also want to thank Dr. Ann English, Dr. Gilles Peslherbe, and Dr. Heidi Muchall for their support and useful suggestions. I am deeply thankful to Dr. Michel Guertin, Dr. Patrick Lagüe and Jean-François Rheault at Laval University for their long interest, deep knowledge and helpful discussions on the microbiology and biochemistry of the truncated hemoglobin N from *Mycobacterium tuberculosis*. I also thank the Fonds de recherche du Québec - Nature et Technologies (FRQ-NT) for funding this research. I also want to thank the Centre for Research in Molecular Modeling (CERMM) at Concordia University and Compute Canada for providing the infrastructure that made this research possible.

Table of Contents

List of Figures

List of Tables

Chapter 1
Introduction

1.1 Mycobacterium tuberculosis (Mtb)

Mycobacterium tuberculosis (Mtb) is a member of the *Mycobacterium tuberculosis* complex – a group of closely related slow-growing mycobacteria, including *M. bovis*, *M. africanum*, *M. microti*, *M. canettii*, *M. pinnipedii*, and *M. caprae*, all agents responsible for tuberculosis [1]. The members of the complex display different phenotypes and mammalian hosts but extreme genetic homogeneity [1]. For many years, it was thought that human tuberculosis evolved from bovine disease by adaptations of an animal pathogen to the human host [2]. It is the current understanding that the complex evolved from a common ancestor – possibly a human pathogen, close parent of Mtb and *M. canettii* – and it underwent an evolutionary bottleneck at the time of speciation, estimated to have occurred approximately 35000 years ago [1]. From the progenitor, *M. bovis* and Mtb lineages branched and evolved independently, with the former expanding its ecological niche to several species and the latter remaining human-specific [1].

Tuberculosis (TB) is one of the oldest recorded human afflictions, established throughout the world 4000 years ago, with the earliest evidence found in Egyptian mummies [3]. It has plagued humankind throughout known history [4]. Archeological, and more recent genetic, evidence of early TB is found in Egypt and South America [4]. Skeletal deformities of TB in Egyptian and Peruvian mummies can be documented more than 4000 years ago [4]. Written records describe TB in India as early as 3300 years ago and in China 2300 years ago [4]. In the 5th century B.C., Hippocrates writes about consumption or phthisis (the classical Greek name for TB) as the most prevalent disease, fatal particularly in young adults [3, 4]. In Europe and North America, TB reaches epidemic proportions during the 18th and 19th centuries due to the growth of large urban centers, an explosion of the population, poor sanitation and housing [4].

A breakthrough in the history and treatment of TB was the research initiated by Robert Koch, the founder of modern bacteriology and 1905 Nobel Prize winner in Physiology and Medicine [4]. Unlike Hippocrates who believed that TB is an inherited disease, Koch elucidated the etiology of tuberculosis reporting Mtb as the causative agent of tuberculosis and established TB as an infectious disease [3, 4]. Mortality rates due to TB steadily dropped at the beginning of the 20th century in the developed world, aided by better public health practices and widespread use of the Bacillus Calmette-Guérin (BCG) attenuated vaccine produced in 1920 by Calmette and Guérin from a virulent *M. Bovis* strain, as well as

the development of streptomycin and isoniazid antibiotics in the 1950s [3]. The most effective first-line anti-TB drug, rifampicin, became available in the 1960s [3].

With the advent of multidrug-resistant Mtb strains and the emergence of AIDS, destroying the immune system of co-infected human hosts, a new TB epidemic started in late 20th century. Contained in Western Europe and North America, Mtb is still a major threat in under-developed countries where TB is mostly spread [3]. The 2013 global tuberculosis report [5] from the World Health Organization (WHO) shows that in 2012, an estimated 8.6 million people developed TB and 1.3 million died of the disease (including 320000 among HIV-infected individuals). 13% of the people who developed TB were HIV-positive [5]. Globally, in 2012 an estimated 450000 individuals developed multidrug-resistant TB (MDR-TB) (i.e. resistance to rifampicin, the most powerful TB drug, and isoniazid) and there were an estimated 170000 deaths from MDR-TB. The majority of cases worldwide were in South-East Asia (29%), African (20%) and Western Pacific (19%) regions [5]. India and China alone accounted for 26% and 12% of the total cases, respectively [5]. The currently recommended treatment for new TB cases is a 6 to 12 month regimen of four first-line drugs: isoniazid, rifampicin, ethambutol and pyrazinamide [5, 6]. Human reluctance to comply with the requisite, intensive 6 to 12 months standard therapy for TB leads still to the ceaseless increasing numbers of antibiotic resistant Mtb strains [5, 7]. The treatment for MDR-TB, defined as resistance to rifampicin, the most powerful TB drug, and isoniazid, is longer and requires more expensive and toxic drugs [5, 7]. For most patients with MDR-TB, the current regimens recommended by WHO last 20 months and treatment success rates are low [5, 7]. The cost of the prescribed antibiotics regimen is prohibitive for the infected and immuno-compromised patients living in under-developed countries where TB incidence rates are highest [5, 6, 7]. The development of novel therapeutic drugs against Mtb and for the treatment of tuberculosis is of utmost importance and extremely urgent. New TB drugs are starting to emerge and combination regimens that include new compounds are tested in clinical trials [5]. Few TB vaccines are also in initial phase of clinical trials [5]. Nonetheless, to date, a vaccine that is effective in preventing TB in adults remains elusive [5]. New TB diagnostics, drugs and vaccines are needed to help end the global TB epidemic.

Mtb infection strategy. The capacity of Mtb to survive and cause disease relies on the bacillus ability to evade the host immune defense mechanisms. Mtb infection of a host is initiated by the inhalation of aerosols, droplets containing a small number of bacilli, expectorated by active pulmonary TB patients [8]. Once in the lung, bacilli penetrate into the terminal alveoli and are engulfed through phagocytosis by alveolar macrophages [8]. In early phase of infection, Mtb internalized by phagocytic immune cells

replicates in a specialized vacuolar compartment called the phagosome [8]. Activated alveolar macrophages (i.e. the condition under which microbicidal activities become upregulated, usually by stimulation of cytokines [9]) can then transfer the phagocytized Mtb to the destructive environment of lysosomes, by fusion of the phagosome with the lysosome to form a mature phagolysosome where the hostile biochemical environment degrades the pathogen [8]. Nonetheless, Mtb has evolved mechanisms to escape the transfer and resist the bactericidal strategy of the macrophages by preventing phagosome-lysosome fusion and survive within the macrophage [8]. Infected macrophages are surrounded and isolated by newly recruited activated macrophages to form the TB characteristic granulomas, structured clusters of various types of immune cells, including macrophages and lymphocytes, with bacilli walled off in the center region [8]. In the granuloma environment, a dynamic balance is established between the Mtb pathogen and the host immune system. In granuloma the persistent bacilli are subject to various stress conditions like hypoxia, nutrient deficiency, acidic pH and inhibition of respiration by nitric oxide [8]. Despite the hostile environment, Mtb evades elimination and survives the stressful conditions mounted by the host immune system by entering a state of dormancy for a prolonged time, even up to the lifetime of the host [8]. In this state of latent infection, TB is asymptomatic. As long as host immunity, in the form of activated macrophages and functional T cells, is effective there is no adverse effect of Mtb on host's health [8]. Defects in cell-mediated immune response resulting form HIV infection, malnutrition, administration of chemotherapy or steroids and anti-tumor necrosis treatment predispose individuals latently infected with Mtb to develop active TB disease [10]. Mtb reactivates in about 1/3 of infected individuals to cause human tuberculosis. Unless treated properly, TB is lethal at this stage [10]. With the decline of the efficacy of the BCG vaccine and the increase in the MDR and XDR-TB cases [5], the development of new strategies for prevention and treatment of tuberculosis is of utmost importance and extremely urgent.

Mtb resistance strategy. Mtb's success as a human pathogen resides in its remarkable capability to compete with and resist the host immunity [8]. Mtb has evolved resistance and survival mechanism both at cellular and biochemical levels [8]. A key Mtb survival strategy is the inhibition of host phagosome-lysosome fusion [8]. Mtb interferes with the fusion process by thickening its cell wall, which in contrast to other bacteria, is made up of unique lipid and glycolipid moieties [8]. This cell-wall composition allows Mtb to modulate transport pathways within macrophages to block delivery of Mtb to lysosomes [8]. Besides interfering with lipid-mediated signaling processed in host macrophages, Mtb survives in the phagosomes and prevents their fusion with lysosomes through production of host-like signaling

molecules, in particular eukaryotic-like protein kinases [8]. Moreover, Mtb has evolved mechanisms to utilize host molecules for their own survival [8].

The capability of Mtb to block the transfer to lysosomes and ultimately its digestion by the host is operational almost exclusively in non-activated macrophages [8]. In activated macrophages, on the other hand, Mtb resists the host destruction in the form of upregulated bactericidal activities such as the generation of various oxidative and nitrosative species (e.g. $O_2^{\bullet -}$ and •NO) [8]. Despite the high toxicity of oxygen and nitrogen reactive species and their continuous production upon macrophage activation, Mtb can persist within this hostile environment, throughout bacillus dormancy [8]. In particular, nitric oxide (•NO), produced by inducible NO-synthases in activated macrophages, plays an important role in the host defense against the microbial pathogen [11] by inhibiting or inactivating key biological processes, including DNA synthesis and respiration [12]. •NO reversibly inhibits cytochrome c oxidases, the terminal enzymes in the respiratory chain [12]. Moreover, •NO combines at near diffusion-limited rate with superoxide ($O_2^{\bullet -}$) produced by respiring cells to form the highly oxidizing agent, peroxynitrite ($OONO^-$) [13]. $OONO^-$ affects respiration by inactivation of the iron/sulfur protein aconitase of the citric acid cycle, the major source of energy in all living systems [12]. In addition, nitrogen dioxide ($\bullet NO_2$), highly reactive derivative of •NO, can effect protein nitration leading to cell death [13]. •NO-metabolizing reactions are imperative for Mtb to fight nitrosative stress. In response to the host defense, Mtb has developed various resistance mechanisms by which the toxic effects of oxygen and nitrogen reactive species can be evaded [8]. Mtb can scavenge oxygen reactive species by a catalase-peroxidase system encoded by the *katG* gene [8]. On the other hand, protection of Mtb against nitrogen reactive species relies on the oxygenated form of a homodimeric truncated hemoglobin N encoded by the Mtb *glbN* gene [14]. The truncated hemoglobin N actively detoxifies •NO to innocuous nitrate (NO_3^-), protects aerobic respiration from •NO inhibition (*in vivo*) [14] and assures Mtb survival in the hypoxic environment of the granuloma or during TB reactivation [15]. All of the above molecular systems are potential targets for the development of new anti-tuberculosis drugs.

1.2 Truncated Hemoglobin N (trHbN) of Mtb

Sequence.

Mtb encodes truncated hemoglobins (trHbs), a class of small oxygen-binding heme proteins widely distributed in bacteria, plants and unicellular eukaryotes and forming a separate cluster within the hemoglobin superfamily [16]. TrHbs display sequences 20-40 amino acids shorter (due to deletions scattered within the sequence) than the classical eukaryotic hemoglobins (Hbs) and myoglobins (Mbs)

and bacterial flavohemoglobins (FHbs), to which they are related by very low sequence similarity [16, 17]. Based on structural features, trHbs in *Mycobacterium* genus have been classified in three groups: group I (also referred as trHbN), group II (trHbO), and III (trHbP). Homology between members of different groups in mycobacteria is insignificant (< 20% identity) [16]. Nonetheless, pathogenic members of the *M. tuberculosis* complex show extremely high identity within the groups [16]. Mtb encodes only trHbN and trHbO proteins. While *glnO* gene is expressed in the growth-phase of the bacterial lifecycle, the *glnN* gene is expressed significantly in the stationary-phase [16], the phase during which the bacterial growth rate slows down as a result of nutrient depletion and accumulation of toxic products. This is one reason that led to the proposition that trHbN and not trHbO of Mtb is best suited to detoxify macrophage-generated •NO by performing O_2/•NO chemistry [18], similarly to bacterial FHbs and eukaryotic Hbs and Mbs [17], which convert •NO to unreactive nitrate, albeit with different efficiencies (see section 1.3).

Fold.

TrHbs tertiary structure is based on a 2-over-2 α-helical sandwich fold, a trimmed domain of the highly conserved 3-over-3 α-helical globin fold [19]. This fold is achieved through truncation of A and F α-helices and specific residue substitutions, resulting in conservation of only B, E, G, and H α-helices of the classical globin fold [19]. The 2-over-2 fold, composed of 2 antiparallel helix pairs, helices B and E on one side, and G and H on the other side, surrounds the heme (Figure 1.1) and confers a relative high rigidity to the overall structure [19]. Hydrophobic contacts between the helices ensure the stability of the truncated fold [19]. Extensive modifications of the conventional Hb/Mb fold occur particularly at the A helix and in the CD-D and EF-F regions of trHbs [19]. A very short segment linking the C and E helices brings the heme-distal E-helix very close to the heme distal site in trHbN relative to classical Hb/Mbs, resulting in close packing of E7, E10 and E11 side chains [16, 19]. The D helix is absent [16, 19]. Critical for the achievement of the 2-over-2 fold in trHb N and O groups is the flexibility given by 3 conserved Gly-based motifs: 2 Gly-Gly pairs located at the beginning of the AB and EF secondary structure transition regions and a Gly immediately preceding the F helix (located next to the protein N-terminus and at both termini of the pre-F proximal loop) [16, 19, 20]. Based on the Gly motifs, the tertiary structure accommodates the deletion of the N-terminal A helix and the replacement of the crucial heme-binding F helix with an extended polypeptide loop [16, 19, 20]. A unique structural feature of trHbN of Mtb is the presence of the Pre-A N-terminal region, which contains a highly polar sequence motif and extends out of the 2-over-2 rigid fold [21].

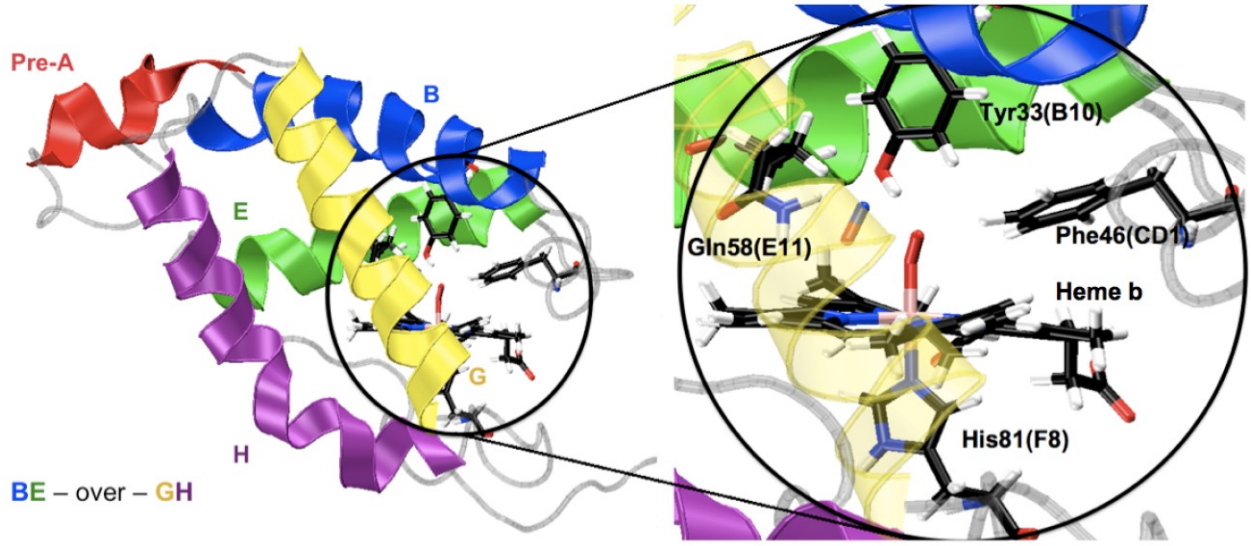

Figure 1.1 Three-dimensional structure of the trHbN of *M. tuberculosis* (PDB: 1IDR). (*Left*) The 2-over-2 α-helical trHb fold formed by helices B (blue) and E (green), and G (yellow) and H (purple), shown in ribbon representation surrounds the distal heme pocket (DHP). (Right) TrHbN active site: O_2-bound heme, proximal His81(F8) conserved in all globins, Tyr33(B10) and Gln58(E11) main ligand stabilizing residues, Phe46(CD1) highly conserved residue protecting the DHP from the solvent and an •NO molecule are represented as sticks. The trHbs nomenclature follows the convention established for sperm-whale Mb: each helix is designated by a letter (A through H starting from the N-terminus) and each residue is numbered based on its position in that helix.

Active site.

The active site of trHbN of Mtb is shown in figure 1.1. It includes the heme b prosthetic group and highly conserved residues discussed below.

The heme-linked proximal HisF8, at position 81 in trHbN of Mtb, is the only perfectly conserved through eukaryotic Hbs and Mbs, bacterial flavoHbs, and trHbs families. In trHbN of Mtb, an unstrained HisF8-Fe coordination stabilizes the heme group. In crystal structure of trHbN of Mtb (PDB ID: 1IDR), His81(F8) imidazole ring is observed in a staggered azimuthal orientation relative to the heme pyrrole N atoms, an orientation which favors the heme in-plane position of the Fe atom and supports fast O_2 association and activation of heme-Fe bound distal ligand through electron donation [16, 19, 20].

The heme distal site cavity of mycobacterial trHbs is characterized by a cluster of highly conserved residues that differ in size and polarity compared to classical eukaryotic Hbs and Mbs, but show little variation compared to bacterial flavoHbs [16, 17, 19, 20].

In trHbs, the distal B10 residue is almost fully conserved as Tyr (the only exception in group I is *N. commune* trHbN, hosting a His residue) [16, 17, 19, 20]. A Tyr at position B10 is also highly conserved in bacterial flavoHbs, while in Mb, for instance, a Leu occupies the B10 position [16, 17, 19, 20].

In trHbs, the E11 residue is mostly Gln, as is in trHbN of Mtb, or Thr, but a Leu in flaboHbs and a Val in Mb. The distal E7 residue, His in most eukaryotic Hbs, can be Leu or Gln in trHbs [16, 17, 19, 20].

In trHbN of Mtb, the E7 position is occupied by a Leu, while in flavoHbs a Gln is found at position E7 [16, 17, 19, 20].

In the crystal structure of oxygenated trHbN of Mtb (PDB ID: 1IDR), the heme-bound O_2 is stabilized by a network of hydrogen bonds between Tyr33(B10), Gln58(E11) and bound ligand [19]. This trHbN-specific hydrogen-bonding network effectively buries the dioxygen O_2 in the distal site and polarizes it to a superoxide character ($O_2^{\bullet -}$) through the H-bond with Tyr33(B10) [19]. In most vertebrate Hbs, HisE7 stabilizes the bound O_2 and there is no H-bonding network as observed in trHbN [16, 17, 19, 20]. The replacement of TyrB10 for HisE7 in modern Hbs and Mbs makes them having a less reactive heme-bound O_2 and better adapted for O_2 transport and storage functions than being efficient catalysts [16, 17, 19, 20]. In trHbN, the H-bonding network confers a greater degree of stability to the heme-bound O_2 ligand by making the O_2 dissociation dependent on multiple, simultaneous H-bonds ruptures [16, 17, 19, 20].

A Phe at the CD1 site is found invariantly, in most eukaryotic globins, bacterial flavoHb, and trHbN of Mtb, but may occasionally substituted by Leu or Tyr in other trHbs [16, 17, 19, 20]. Its main role is shielding the distal heme pocket of all globins from the solvent.

In trHbs, other relevant residues are E15, G8 and B9 [16, 19, 20].

E15 is mostly Leu but Phe in group I trHbs [16, 19, 20]. Phe62(E15) of trHbN from Mtb has been reported to be the main gate for O_2 diffusion into the distal heme pocket [22]. By changing conformations, Phe62(E15) opens ligand access from inside the protein matrix into the distal cavity [22]. Ligand diffusion to/from the distal heme site via the 'E7 gate', as observed for sperm whale Mb, where HisE7 swings and opens ligand access to the heme, is precluded in trHbN due to the close packing of Leu54(E7), Lys57(E10) and Gln58(E11) side chains in the distal pocket (see above) [16, 17, 19, 20].

A Val occupies the G8 position in trHbNs, including that from Mtb, but can be Trp or Ile in trHb O and P groups, and a Phe at position B9 is highly conserved in trHbNs. In flavoHbs as in trHbNs, Val and Phe also occupy the G8 and B9 positions, while in Mb Ile occupies both positions [16, 17, 19, 20].

In trHbN of Mtb, Phe32(B9), Val94(G8), and Gln58(E11) residues control the traffic in or out of the heme pocket cavity [23].

Such a selection of distal site residues, instrumental in achieving the trHb-specific hydrogen-bonded distal site network that stabilize the heme-bound ligand through interactions with Tyr(B10) and the neighboring E11, E7, CD1, G8, and B9 side-chains, and the large size of the distal heme pocket, alike those in bacterial flavoHBs, compared to the small pockets of modern Hbs and Mbs [16, 17, 19, 20], are key factors in making trHbN from Mtb an efficient of •NO scavenger.

Tunnels.

Despite their 'truncated' polypeptide chain, trHbs display and inner hydrophobic tunnel/cavity system that supports ligand diffusion to/from the distal heme pocket (DHP), storage of apolar diatomic ligands (i.e. O_2 and •NO) within the protein matrix and release of polar species (e.g. NO_3^-). trHbN of Mtb hosts multiple apolar tunnels inside its protein matrix formed by dynamic reshaping of short-lived hydrophobic cavities of sufficiently large volumes to accommodate few small, low-polarity ligands and making them accessible to the active site [23]. Daigle et al [23] showed that the relatively high structural rigidity of trHbN backbone enables the formation of the cavities and allows trHbN to support the tunnels without collapsing. The cavities were found to correspond to experimentally determined xenon binding sites and act as transient ligand docking sites. They are temporarily interconnected due to side chain flexibility and steric barriers dictate the passage from one cavity to another [23]. The crystal structure of oxygenated trHbN [19] showed 2 tunnels that link the buried DHP to the bulk solvent the long (LT) and short (ST) tunnels, respectively (Figure 1.2). The LT has a length of 20 Å, has the biggest average volume, and extends from the solvent along the protein matrix between helices B, E and G. The ST has a length of 13 Å and is situated between the G and H helices [19]. Molecular dynamics simulations of Daigle et al [24] revealed 2 additional tunnels named EH and BE after the helices in between which the tunnels reach the solvent. The BE tunnel extends from between the highly conserved Tyr33(B10) and Phe46(CD1) side chains to the solvent. Tyr33(B10) backbone is found at its entrance. BE tunnel has a length of 10.5 Å and it is the narrowest trHbN tunnel particularly at the protein surface.

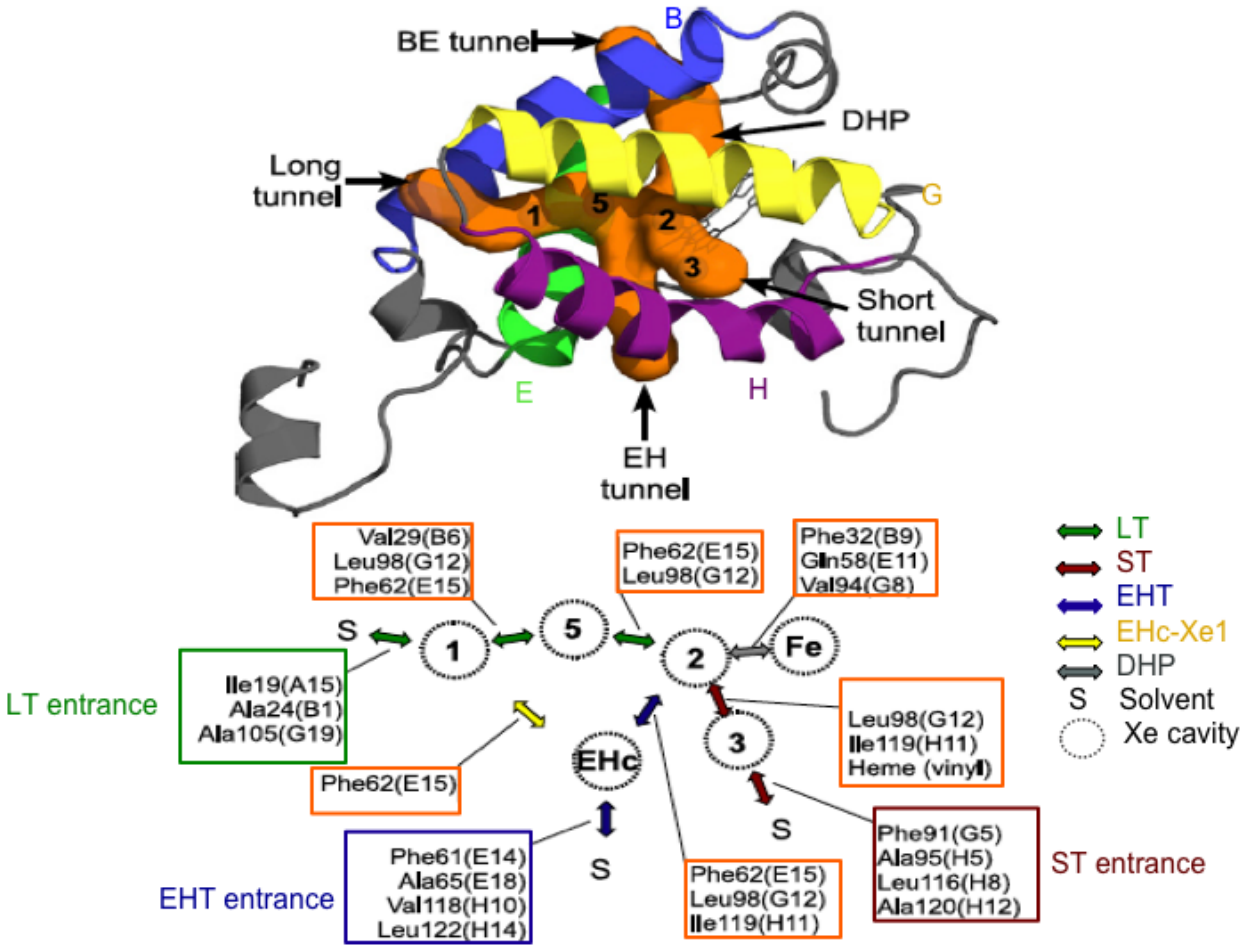

Figure 1.2 The tunnel/cavity system of trHbN (PDB: 1IDR, subunit A). (*Top*) The tunnels: long (LT), short (ST), EH tunnel (EHT), and BE tunnel (BET), are represented by an orange surface. (*Bottom*) Map of ligand diffusion pathways: The ligand/substrate diffusion routes from one xenon cavity to the other (circles) are represented as arrows (green, red and blue for diffusion in LT, ST, and EHT, respectively). Diffusion into the distal heme pocket (DHP) from xenon cavity 2 is represented as a grey arrow. The schematic includes the hydrophobic residues at tunnel entrances (green, dark red, and blue boxes for LT, ST, and EHT, respectively and those dynamically reshaping the trHbN cavities (orange boxes). See text for details. Adapted with permission from Daigle, R., Rousseau, J. A., Guertin, M., and Lagüe, P. (2009) Biophys. J. 97 (11), 2967-2977 [23]. Copyright © 2009 Biophysical Society. Published by Elsevier Inc.

Ligand/substrate diffusion toward trHbN active site starts with favorable hydrophobic interactions at specific trHbN surface sites, composed of clusters of hydrophobic residues at tunnel entrances (Figure 1.2 green, dark red and blue boxes) [23]. Once captured, O_2 and •NO diffuse inside the trHbN matrix by hopping from Xe cavity to Xe cavity (Figure 1.2 circles), dynamically reshaped by changes in side-chain conformations of specific hydrophobic residues (Figure 1.2 orange boxes) [23]. For instance, Daigle et al's simulations in aqueous solution [23] showed that •NO significantly alters the dynamics of key amino acids: Phe62(E11), a residue proposed to act as a gate controlling ligand traffic inside LT (main O_2 gate) [22] and Ile119(H11) controlling ligand traffic inside ST toward Xe2 binding site [23]. From the Xe2 binding site located at the intersection of the ST, LT and EH tunnels, the ligands reach the DHP cavity and are available for catalysis [23]. Access to the heme pocket cavity is controlled by the highly-conserved residues: Phe32(B9), Val94(G8) and Gln58(E11) [23].

Discrepancies exist in the literature regarding the various ligand diffusion pathways and the influence of trHbN environment on ligand diffusion to the active site and thus the efficiency of the trHbN catalytic activity, the nitric oxide dioxygenase (NOD) reaction (see section 1.3). For instance, a dual-path mechanism has been suggested for migration of O_2 and •NO to the heme where O_2 entry and diffusion through deoxy-trHbN occurs only via ST and where O_2 binding to the heme triggers conformational and dynamical fluctuations of the protein especially those of the Tyr33(B10)-Gln58(E11) pair and around Phe62(E15), promoting the opening and •NO migration through LT [22]. This mechanism has been conclusively refuted however. Daigle et al's simulations [23] showed that the presence or absence of a coordinated O_2 molecule does not control the opening of LT but the opening of the EH tunnel, and that •NO diffusion though LT is hindered by Phe62(E15) [23]. The high energetic barrier created by the obstruction is bypassed by the use of EH tunnel [23]. Moreover, ST has been found to be the preferential channel for •NO capture and diffusion to oxy-trHbN heme pocket [23]. This is due to the presence of its funnel-shaped entrance which triggers the frequent formation of solvent-excluded cavities capable of hosting up to 3 •NO molecules, with no escape back into the solvent, thereby accelerating •NO capture, entry and delivery to the active site for catalysis [23]. In addition, ST displays the shortest diffusion length, thus assuring the fastest •NO delivery to the active site for catalysis [23]. Similarly, the release of NO_3^- has been suggested to occur through the hydrophobic BE tunnel [25]. Nonetheless, given the size and the charge of NO_3^-, its diffusion out of the active site is favored through the polar LT [23].

Membrane association.

The Pre-A N-terminal region (Figure 1.1) and the multiple tunnel/cavity system are trHbN-specific structural features that greatly contribute to the high-efficiency of the trHbN biological activity. For instance, the deletion of the Pre-A highly polar sequence motif significantly alters trHbN dynamics and conformational state of Phe62(E15), the 'main gate' for ligand diffusion, thus restricting the passage to DHP and greatly impairing the ability of trHbN for •NO detoxification [23]. Moreover, Daigle et al's simulations [23] showed that the hydrophobic character of the multiple trHbN tunnels entrances, the diffusion path lengths from the tunnel entrances to the DHP, and the dynamic formation of the hydrophobic cavities inside the protein matrix, ensure efficient •NO capture and fast delivery to the active site preferentially through the short tunnel (ST), and ultimately the efficiency of the trHbN catalyzed NOD reaction. It has been shown that mutations at tunnel entrances slow down the NOD reaction (see section 1.3) mainly by limited access of •NO to DHP (Michel Guertin, personal communication).

Studies on the solubility of O_2 and •NO molecules show that their solubility is three times greater in biological membranes than is aqueous solution [26]. The opposite is observed for nitrate, the product of the NOD reaction [26]. Moreover, a few insights suggest that trHbN might interact with the membrane. During trHbN purification process, 10-20% of trHbN of Mtb remains bound to the membrane fraction (Michel Guertin, unpublished results). Membrane protein explorer (MPEx) tool [27], starting from trHbN amino acid sequence, predicts two membrane segments by which trHbN can interact with the membrane surface. These segments encompass the entrance to the BE tunnel and a good part of the ST entrance. However, very little is known on the nature of trHbN-membrane interactions and the molecular mechanism of ligand capture from membranes.

Nonetheless, a recent combined spectroscopic and computational study of Rheault et al (manuscript in preparation) shows that trHbN of Mtb is a peripheral membrane protein, and that its association with model membranes, representative of mycobacterial plasma membrane and mammalian cell membranes, occurs via the Pre-A, G and H helices. It is believed that the Pre-A segment is always bound to the membrane, ensuring that trHbN is near the source of small apolar ligands, while the trHbN core modulates the binding to the membrane via the electrostatic interactions between the lipid membranes and the Asp100 residue, located on the G helix. In its membrane-bound form, the ST tunnel, situated between G and H helices, is oriented toward the membrane interior, and the other tunnels are pointing toward the solvent. Such an orientation would facilitate the uptake of nonpolar substances from the membrane and release of the charged product to the solvent. Their results confirm an earlier hypothesis that trHbN of

Mtb is an amphitropic protein [28] that exists both in solution and associated with lipid membranes, and is capable of maintaining its structural integrity and catalytic activity in two such diverse environments.

1.3 Nitric Oxide Dioxygenase Reaction

1.3.1 trHbN Function

The truncated hemoglobin N (trHbN) of *M. tuberculosis* prevents the irreversible oxidation and nitration of the heme protein by metabolizing •NO to innocuous NO_3^- through the rapid nitric oxide dioxygenase (NOD) reaction:

$$\mathbf{trHbN\text{-}Fe^{II}\text{-}O_2 + {}^{\bullet}NO \rightarrow trHbN\text{-}Fe^{III} + NO_3^-}$$

TrHbN also prevents the release of highly reactive and toxic $OONO^-$ and $\bullet NO_2$, proposed intermediates in the NOD reaction mechanism.

The NOD reaction is central to the defense system of Mtb, for coping with the toxic effects of elevated levels of •NO ([•NO] = 0.1 – 1 μM) in the hypoxic environment of the granuloma ([O_2] = 1 – 4 μM) [14, 15].

Overall NOD reaction rate.

TrHbN catalyzes the rapid oxidation of •NO to the unreactive NO_3^- with a second-order rate constant: k_{NOD} = 7.45 x 10^8 M^{-1} s^{-1} (23 °C), close to that of reactions limited by diffusion of substrates (6.9 x 10^9 M^{-1} s^{-1}) [14]. This rate is one of the largest relative to other globins functioning as NODs (Table 1.1). The NOD reaction in trHbN is more than twenty-fold times faster than in sperm-whale Mb and human Hb, but three-fold times slower compared to the NOD reaction catalyzed by microbial flavoHbs of *E. coli* and *A. eutrophus,* the most efficient •NO dioxygenases studied so far.

Table 1.1 Comparison of •NO dioxygenation kinetic constants and elementary rate constants for ligand binding of *M. tuberculosis* truncated hemoglobin N (TrHbN), bacterial *E. coli* and *A. eutrophus* flavohemoglobins (FlavoHbs), and mammalian sperm-whale myoglobin (SW Mb) and human red blood cell hemoglobin (RBC Hb).

Rate constant	TrHbN[a]	FlaboHbs[b]	SW Mb[c]	RBC Hb[d]
k_{NOD} ($\mu M^{-1} s^{-1}$)	745	900 – 2900*	34 – 43	50 – 89
K_d (O_2) (nM)	8	4 – 36	710 – 880	>1000
k'_{O2} (s^{-1})	25	17 – 50	14 –17	10 – 20
k_{O2} ($\mu M^{-1} s^{-1}$)	0.2	0.2 – 0.6	12 – 15	9 – 24
K_d (•NO) (pM)	–	8 – 20	5	2
$k'_{\bullet NO}$ (s^{-1})	–	10 – 26	17 – 22	25
$k_{\bullet NO}$ ($\mu M^{-1} s^{-1}$)	–	0.0002	0.0001	0.00005

* Rate constants were determined at 37 °C. All other rate constants were reported at room temperature.

[a] From [14, 15].

[b] From [17].

[c, d] From [29].

Ligand binding rates.

O_2 binding to ferrous heme is essential for the NOD reaction and trHbN function. TrHbN has a high O_2 affinity: K_d = 8 nM (at physiological [O_2] = 10-15 μM and [•NO] = 1-2 μM), one of the largest among globins, which enables the NOD reaction under O_2 and •NO concentrations prevailing in infected lesions ([O_2] = 1 – 4 μM and [•NO] = 0.1 – 1 μM) [14]. This is due to a small dissociation constant, k_{O2} = 0.2 s^{-1}, as small as that of the enzymatic flavoHbs [17]. In contrast, O_2 dissociation constant is much larger for the human Hb and sperm-whale Mb [29] which are rather inefficient •NO dioxygenases and are better adapted for their modern O_2 transport and storage function. The rate constant for O_2 binding is 25 $\mu M^{-1}s^{-1}$, comparable to the association rates determined for flavoHbs, human Hb and sperm-whale Mb [14, 17, 29]. A large O_2 affinity is thus critical for an efficient •NO dioxygenase activity.

The O_2 affinity of the above-mentioned globins is largely determined by dielectric and steric influences within their distal heme pocket (DHP) structure and hydrogen bonding residues that stabilize the bound O_2 [17]. TrHbN, like flavoHbs, displaying large and low polarity DHPs have small k_{O2} and high O_2

affinity. Human red blood cell Hb and muscle Mb, on the other hand, with small polar DHPs have large k_{O2} values and much lower O_2 affinity. As already mentioned, distal Tyr33(B10) in trHbN and flavoHbs, and His(E7) in red blood cell Hb and muscle Mb, play key roles in stabilizing the bound O_2 via H-bonding (and in determining O_2 affinity). For instance, loss of H-bonding by Tyr(B10) in *E.coli* flavoHb and His(E7) in RBC Hb and SW Mb increases the O_2 dissociation constant (k_{O2}) by greater than 60-fold, while showing lesser effect on the association constant (k'_{O2}) [17]. Similarly, kinetic analysis of the Tyr33(B10)Phe mutant in trHbN of Mtb showed a 150-fold increase in O_2 dissociation rate, thus substantially decreasing O_2 affinity [14].

Competition between •NO and O_2 for binding the ferrous heme can inhibit the NOD activity of many Hbs. For flavoHbs, human Hb and sperm-whale Mb, the •NO association and dissociation constants have been determined and show similar rates, indicating little adaptation of their heme pockets for •NO binding [17]. A 60-fold lower O_2 affinity of the Tyr(B10)Phe mutant in *E.coli* flavoHb (see above) results in a profound susceptibility to •NO inhibition [17]. Steady-state assays of NOD activity in flavoHbs showed, though, a weaker •NO inhibition [30]. By binding O_2 with high affinity, flavoHbs avoid •NO inhibition by decreasing •NO binding to the heme [30]. *For trHbN of Mtb, the rate constant for •NO binding has not yet been determined*. Nonetheless, given the almost equal O_2 dissociation rates and cluster of distal residues stabilizing the bound ligand, it can only be inferred that trHbN discriminates against •NO by a similar mechanism, due primarily to its large O_2 affinity.

The dual-path mechanism for O_2 and •NO diffusion to the heme pocket (see section 1.2, tunnels), in which O_2 binding to the heme allosterically modulates •NO capture and availability by triggering the opening of a specific •NO trHbN tunnel, was suggested as 'the most attractive explanation' [12] for how trHbN discriminates between O_2 and •NO ligands binding to the heme and achieve the most efficient •NO detoxification (the different O_2 and •NO tunnels switching was found to occur on picoseconds to nanoseconds timescale) [17, 22]. Nonetheless, the dual-path mechanism has been contradicted. It has been shown [23] that it is not the allosteric modulation of tunnels dynamics, but the hydrophobic character of the multiple trHbN tunnels entrances, the dynamic reshaping of hydrophobic cavities inside the protein matrix, the diffusion path lengths to the heme pocket, and the orientation of the tunnels with respect to the trHbN membrane, that are responsible for •NO capture, fast delivery to the active site, preferentially through the short tunnel, and ultimately the efficiency of the trHbN catalyzed NOD reaction. Indeed, mutations of hydrophobic residues at tunnel entrances designed to increase polarity, such as Ala24(B1) at the entrance of LT, Ala120(H12) at the entrance of ST, and Val118(H10) at the

entrance of EHT, to polar Ser or Asp residues, decrease ligand binding affinity and reduce trHbN activity [23]. Mutations designed to obstruct the tunnel entrances while maintaining their hydrophobic character, such as Ala24(B1) at the entrance of LT, Ala95(G9) at the entrance of ST, Ala65(E18) at the entrance of EH tunnel and their double and triple combinations, to bulky Leu or Ile amino acids decrease ligand association and dissociation rates and slow down the NOD reaction (e.g. 3-fold reduction of NOD reaction rate for the triple LT/ST/EHT mutation) mainly by limited access of •NO to DHP (Michel Guertin, personal communication).

In summary, the large O_2 affinity and the complex trHbN hydrophobic tunnel/cavity system are critical for the efficient trHbN •NO dioxygenase activity. The large O_2 affinity is due to the trHbN large heme pocket lined up with highly conserved residues that stabilize and activate the O_2 ligand. The trHbN hydrophobic tunnel/cavity system allows fast entry of the •NO substrate and provides direct access to the bound O_2 in the active site. It is commonly agreed [16-30] that the diffusion-controlled migration of the ligands to the DHP is the slowest process and thus the rate-limiting step in the •NO detoxification, regardless of the NOD reaction mechanism.

1.3.2 Mechanism

The general proposed overall mechanism of the NOD reaction (Figure 1.3) comprises five steps:

(1) O_2 binding to ferrous iron to form a ferric superoxide complex essential for the •NO attack,

(2) reaction of free •NO with the ferric superoxide complex to form a peroxynitrite intermediate complex,

(3) isomerization of the peroxynitrite complex to form a heme-bound nitrato-complex,

(4) dissociation of the Fe-O bond and release of the nitrate anion, and

(5) reduction of the ferric form to the ferrous O_2-binding form.

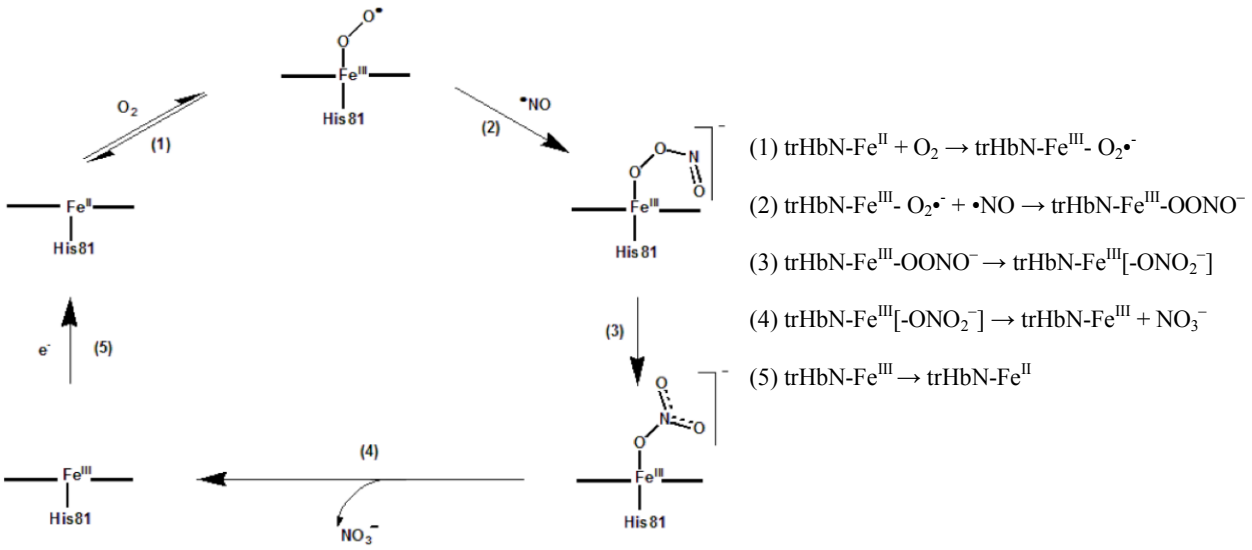

Figure 1.3 Overall NOD reaction mechanism. The reaction steps are described in the text.

As previously mentioned, peroxynitrite $OONO^-$ is highly reactive and toxic as it can oxidize and/or nitrate all major types of biomolecules including DNA, proteins and lipids. Therefore, to be effective the isomerization reaction must be rapid. Moreover, the isomerization reaction may involve the formation of transient radical intermediates, which can be quite harmful if they escape the active site. To this day, two mechanisms have been considered for the NOD isomerization reaction:

(1) a *sequential* mechanism (trHbN- Fe^{III}-$OONO^-$ → trHbN-[Fe^{IV}=O^{2-}] + •NO_2 → trHbN-Fe^{III}[-ONO_2^-]) (Figure 1.4 1) that involves the homolytic cleavage of the O-O bond of the peroxynitrite complex to produce (caged radicals) oxo-ferryl species (compound II) Fe^{IV}=O^{2-} and •NO_2 radical intermediates (Figure 1.4 1a), followed by the •NO_2 radical attack on the oxo-ferryl species to form the heme-bound nitrato-complex (Figure 1.4 1b), and

(2) a *concerted* mechanism (trHbN- Fe^{III}-$OONO^-$ → trHbN-Fe^{III}[-ONO_2^-]) (Figure 1.4 2) that involves an internal rearrangement reaction from the peroxynitrite complex to the heme-bond nitrato complex in which the eroxo O-O bond is simultaneously ruptured as the iron-bonded O-atom bonds nitrogen to form bound nitrate.

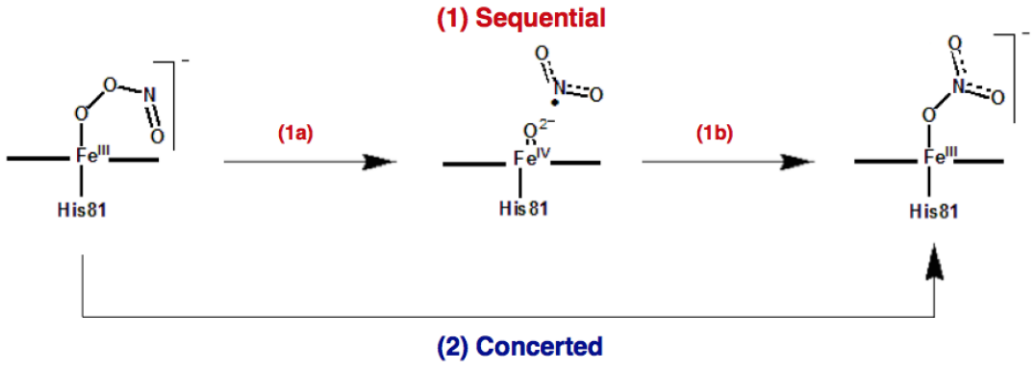

Figure 1.4 Mechanisms of NOD peroxynitrite isomerization reaction.

Theoretical calculations of Blomberg et al [31] suggested the sequential mechanism for mammalian Mb and Hb. In their models of the NOD reaction in Mb employing electronic structure calculations Blomberg et al [31] reportedly failed to find a concerted mechanism yielding plausible activation energies, supporting the sequential mechanism given a relatively low energy barrier for the O-O bond homolysis and a highly exergonic overall reaction sequence. *In trHbN of Mtb both mechanisms have been proposed*. For instance, Crespo et al's QM/MM geometry optimizations [32] support the sequential mechanism. In their calculations, both elementary steps: the O-O bond homolysis, and formation of bound nitrate from oxo-ferryl species and $\bullet NO_2$, led to very low activation barriers and both processes were highly exergonic. On the other hand, Mishra et al [33] proposed the concerted mechanism given that, during their adiabatic reactive molecular dynamics (ARMD) simulations, the $OONO^-$ homolytic cleavage and $\bullet NO_2$ dissociation elementary step did not occur. While there is general consensus [32, 33] on the fact the formation of the peroxynitrite complex from the reaction of free •NO with the ferric superoxide complex yields rate constants on picoseconds timescale, *substantial differences exist with respect to the time constant of the isomerization step*: picoseconds for the concerted mechanism [33] compared to microseconds for the sequential mechanism which would not explain the rapid overall NOD reaction rate [32]. Though Mishra et al [33] found strong evidence that the concerted mechanism is favorable in view of energetics, reaction rate and geometrical properties comparable with electronic structure calculations, they indicated, however, that a more detailed analysis of the $OONO^-$ homolysis elementary step is required before ruling out the sequential mechanism given that observing $\bullet NO_2$ dissociation in the sequential mechanism depended on the force field parameters used in their simulations. Nonetheless, the concerted mechanism

may be favored given that it does not involve highly reactive radical species that could lead to the degradation of the protein.

Experimental studies on the •NO dioxygenation in Mb and Hb provide conflicting and inconclusive views on the mechanism and possible intermediates of the NOD reaction. For instance, Herold et al [29, 34, 35] using rapid scan UV-vis spectroscopy provided evidence for a millisecond-lived peroxynitrite Fe(III)$OONO^-$ intermediate in both oxy-Mb and oxy-Hb. They were unable to detect any dissociated $•NO_2$ but observed quantitative nitrate formation and suggested that the peroxynitrite coordinated to ferric iron undergoes a rapid rearrangement to nitrate (without nitrating the globin residues). Their analysis is inconclusive, however, on whether the rearrangement is concerted or not since the lack of detection of oxo-ferryl species and $•NO_2$ may either indicate that the intermediates are not formed at all or that they react too fast to accumulate and be detected experimentally. Moreover, Yukl et al [36] using resonance Raman spectroscopy and rapid-freeze quench techniques showed that the millisecond intermediate found by Herold et al [29, 34, 35] in the reaction of •NO with oxy-Mb is an Fe(III)-nitrato complex, not a peroxynitrite, and mentioned that their results do not invalidate the sequential mechanism. In addition, Bourassa et al [37] proposed O-O homolysis based on stopped-flow kinetic measurements, and Groves et al [38] provided evidence for ferryl-Mb formation from met-Mb and $OONO^-$ by spectroscopic detection. *As far as possible intermediates of the NOD isomerization reaction are concerned, there have been no experimental kinetics studies for trHbN.*

The role of active site residues in the NOD reaction in trHbN of Mtb has been investigated mainly by computational approaches. *Discrepancies exist* between Crespo et al [32] and Mishra et al [33] findings *about the role of the trHbN environment in assisting the NOD isomerization reaction*. Mishra et al [33] assessed the role of the active site residues through ARMD simulations of Tyr33Ala and Gln58Ala mutants and their combination. Similarly to the wild-type trHbN, the $OONO^-$ homolysis reaction did not occur in the variants. However, their simulations revealed that $•NO_2$ rebinding elementary step of the sequential isomerization reaction is not entirely diffusion-controlled, but instead is strongly influenced by Tyr33(B10) and Gln58(E11) residues which pre-orient the reactive ligands through a highly dynamical H-bonding network. For instance, the Tyr33Ala mutation leads to a significant retardation in the •NO dioxygenation: the time constant differed by an order of magnitude from the wild-type trHbN. (Mishra et al's concerted rearrangement mechanism [33] was found to be strongly influenced by the mutation of Tyr33(B10) residue whereas Gln58(E11) residue was found to have rather small effects on the reaction.) This is in agreement with Ouellet et al's experimental study [14] using a Tyr33Phe mutant that showed an

increase in $\bullet NO_2$ dissociation rate and a decrease in •NO dioxygenation rates in the mutated protein compared to wild-type trHbN. This is contrary to Crespo et al's study [32], using also a Tyr33Phe mutant, reporting that the trHbN environment does not make significant contributions to the heme moiety catalyzed reaction. However, Crespo et al [32] suggested (based on similarities with flavoHbs) that the active site residues, especially the Tyr33(B10)/Gln58(E11) pair, might be relevant to the physiological function of trHbN at different levels, including isolating the reaction intermediates formed transiently in the hydrophobic pocket formed by Phe32, Tyr33, Val36, Phe46, and Val94 unlike in water solution where the $\bullet NO_2$ radical may escape and react with other species in solution [17, 32].

One possible origin for the different conclusions of the two theoretical studies concerning the role of the trHbN environment may be that the QM/MM calculations of Crespo et al [32] employed restrained energy minimizations along predefined reaction coordinates, while ARMD employed by Mishra et al [33] allows for fully flexible and sufficiently long explicit molecular dynamics simulations. Crespo et al's [32] method introduces an additional term in the potential energy of the system to penalize any deviation of a reaction coordinate from a reference value. Moreover and importantly, it lacks nuclear dynamics and conformational sampling. Mishra et al's [33] ARMD method is a simple potential energy surface crossing approach to study reactive processes, involving bond breaking and bond forming, within the classical MD framework. The method involves the parameterization of potential energy surfaces of the reactants and the products with individual force fields and the energy difference between the reactant and product states is a free parameter.

Due to the presence of Tyr33(B10) in trHbN active site, that could supply the redox equivalent needed for catalyzing the O-O bond cleavage, Yeh et al [18] hypothesized a mechanism in which Tyr33(B10) could be directly involved in the NOD isomerization reaction. This mechanism involves the heterolytic O-O bond cleavage of the peroxynitrite complex to produce compound I oxo-ferryl intermediate, a Tyr33(B10) radical cation (Tyr33$\bullet^+$), and the nitrite NO_2^- anion.

$$\text{trHbN-Fe}^{III}\text{-OONO}^- \rightarrow \text{trHbN-[Por}\bullet^+\text{-Fe}^{IV}\text{=O}^{2-}\text{]} + NO_2^- \rightarrow \text{trHbN-[Fe}^{IV}\text{=O}^{2-}\text{]Tyr}\bullet^+ + NO_2^- \rightarrow$$

$$\text{trHbN-[Fe}^{IV}\text{=O}^{2-}\text{]} + \bullet NO_2 \rightarrow \text{trHbN-Fe}^{III}\text{[-ONO}_2^-\text{]}$$

In this alternative reaction path, compound I complex (where an unpaired electron is on the porphyrin ring) is reduced by the nearby Tyr33(B10) (i.e. the iron receives one electron from Tyr33) to generate compound I and the Tyr33(B10) radical cation (the unpaired electron is on Tyr33 instead). The Tyr33(B10) radical cation is then re-reduced by NO_2^- to form compound II and $\bullet NO_2$ radical, and the

reaction continues as in the sequential mechanism with $\bullet NO_2$ radical attack on compound II to form the heme-bound nitrato-complex.

Crespo et al's study [32] indicated that Tyr33(B10) does not play a catalytic role in the NOD reaction given that the reaction energy profiles obtained for wild-type trHbN were very similar to those obtained for the Tyr33Phe mutant, indicating instead that the trHbN catalyzed the NOD reaction occurs mainly by means of the heme group. It should be noted that, Herold et al [29, 34, 35] suggested that the relatively slow reaction of $\bullet^{+}$HbFe(IV)=O with NO_2^- (16 $M^{-1}s^{-1}$) and the rapid reaction of HbFe(IV)=O with $\bullet NO_2$ (10^7 $M^{-1}s^{-1}$) favor the mechanism involving homolysis of the peroxynitrite O-O bond to produce $\bullet NO_2$ over the heterolytic mechanism producing NO_2^-.

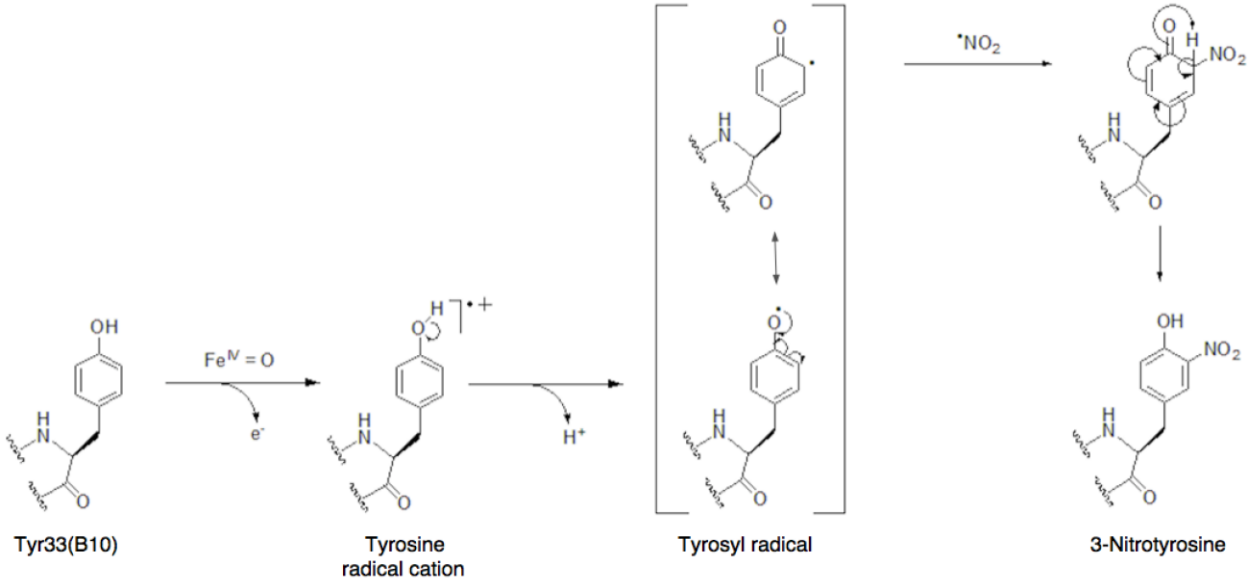

Figure 1.5 Mechanism of Tyr33(B10) nitration. Only two out of the four possible resonance forms of tyrosyl radical are depicted.

The presence of Tyr33(B10) and of highly reactive species in the active site is also problematic in that it could lead to trHbN permanent degradation. $Fe^{IV}=O^{2-}$ is a strong oxidant (~1.0 V) [13] that could readily react with Tyr33(B10) to form a tyrosyl radical (Tyr33•) and a ferric heme with hydroxide bound (Fe^{III}-OH^-), first by one electron transfer from Tyr33 to the ferryl iron to form to form a tyrosine radical cation (Tyr33$\bullet^{+}$) followed by proton abstraction from Tyr33 hydroxyl group by the ferric heme to form the tyrosyl radical (Tyr33•) (see figure 1.5). The Tyr33• radical can also irreversibly interact with $\bullet NO_2$ to form 3-nitrotyrosine (see figure 1.5) that could lead to permanent trHbN degradation and potentially the

death of Mtb bacillus. *How trHbN prevents these possible secondary reactions (i.e. Tyr33 oxidation and nitration) is a critical issue and has not been considered to this day in theoretical studies.*

Regardless of the NOD isomerization mechanism, Gardner et al [39] have reported high fidelity incorporation of both O-atoms of O_2 in nitrate in reactions of •NO with *E. coli* flavoHb$^{18}O_2$, human red blood cell Hb$^{18}O_2$ and sperm-whale Mb$^{18}O_2$ (in contrast to the non-enzymatic reaction of •NO with indolamine dioxygenase-like, structurally unrelated Mb-Fe$^{II}O_2$ from the mollusk *Turbo cornutus*, or free superoxide radical (O_2•$^-$) both low fidelity). Their electrospray mass spectrometry measurements and analysis showed > 99% double O-atom incorporation into NO_3^- at physiological pH value of 7.5. For comparison, only ~87% O-atom retention occurs during the isomerization of HOONO in aqueous solution, indicating water O-atom incorporation. *No similar experimental mass balance studies accounting of NO_3^- product have been reported for trHbN*.

Dissociation of the nitrate anion, the product of the NOD reaction, involves the breaking of the bond between the anion and the heme group, and a change in the iron coordination from hexa- to penta-coordinated. The release of the nitrate anion to the aqueous environment involves two processes: 1) the breaking of the Fe^{III}-O bond in the heme-bound nitrato complex, and 2) the diffusion of the anion through the protein matrix. Marti et al [25] simulated the release of the nitrate anion by Mtb trHbN. *Their molecular dynamics simulations suggest that the formation of the ferric-nitrato species causes a structural distortion of the distal heme pocket cavity walls forming pores for water entry. The structural destabilization affects, among other residues, Phe46(CD1), the residue that shields the heme from the solvent, the side-chain of which rearranges to open a pathway for water entry.* Moreover, their QM/MM energy minimizations suggest that water hydration weakens the bond between the heme iron atom and nitrate anion [25]. Once the Fe^{III}-O bond is broken, the nitrate anion exits in ~5 ns [25]. A role for ThrE2 in assisting nitrate egress has been proposed [25]. Furthermore, Marti et al's QM/MM energy minimizations pointed out that the Tyr33(B10)/Gln58(E11) pair is crucial for breaking the Fe^{III}-O bond of the heme-bound nitrato complex [25]. Similarly, Mishra et al's ARMD simulations [33] with trHbN and its mutants Tyr(B10)Ala and Gln(E11)Ala indicated that Tyr33(B10) and Gln58(E11) strongly influence nitrate dissociation. *The stabilization role of the highly conserved aromatic Phe46(CD1) and Phe32(B9) residues in promoting product dissociation has never been addressed in their studies*. Nonetheless, electronic structure calculations, surveys of crystallographic data, and experimental binding energies reported by Bryantsev and Hay [40] show that benzene forms C−H hydrogen bonds with nitrate NO_3^- anion that can exceed 57% of the strength of those formed by O−H group from water, and when present

in a receptor (i.e. aromatic side chains in trHbN active site), C−H groups could considerably enhance anion binding affinity and they should be considered as additional binding sites within the host cavity.

Univalent reduction of the ferric heme to the ferrous form the only one that binds O_2 – the last step in NOD reaction cycle – is essential for rapid turnover. Lack of a suitable reductase to drive the NOD catalytic cycle diminishes the capacity of various Hbs and Mbs to function as NODs [17]. Unlike flavoHbs, the most efficient NODs, which have a reductase domain besides the globin domain, *an associated reductase for trHbN of Mtb has not yet been identified*.

1.4 Research objectives

This Master's thesis consists of a theoretical study of the NOD reaction in trHbN from Mtb. The fact that experimental studies of the NOD reaction in trHbN are rather scarce and that existing computational studies, differing in the methodologies used, provide conflicting and inconclusive views on the mechanism, energetics and dynamics of this system, prompted us to investigate this challenging reaction using state-of-the-art computational approaches (see methods). The study aims to:

1) elucidate the peroxynitrite isomerization mechanism;

2) determine the interactions of trHbN active site residues that are significant for the isomerization reaction;

3) understand what prevents Tyr33(B10) nitration and the permanent degradation of trHbN itself; and

4) understand the role of trHbN active site residues in nitrate dissociation and release.

Chapter 2
Computational methods

2.1 Gas-phase model of NOD reaction

Quantum mechanical (QM) electronic structure calculations at high-level density functional theory (DFT) were employed here to explore the NOD reaction mechanism in gas phase. All calculations were performed with Gaussian 09 quantum chemistry code [41].

A minimal model was used to investigate the •NO attack on heme-bound O_2 and the subsequent isomerization of the peroxynitrite intermediate to heme-bound nitrate. The heme group was modeled as a porphyrin ring without the heme substituents (i.e. excludes the propionates, vinyl, and methyl groups). The proximal histidine, His81(F8) was modeled as an imidazole ring. The model system contains the Fe-porphin complex, the O_2 bound to the Fe atom, the imidazole ring and the •NO substrate. To build the model the crystal structure of oxy-trHbN (PDB ID: 1IDR) was used as the starting point.

QM(DFT) can provide a potential energy surface (PES) on which stationary points can be located and the full range of possible reactions involving $OONO^-$ and $\bullet NO_2$ intermediates can be captured. Two reaction coordinates have been selected for the construction of a two-dimensional (2D) PES for the peroxynitrite isomerization step of the NOD reaction (Figure 2.1): 1) O1-O2 distance to describe the cleavage of the O-O peroxo bond of the heme-bound $OONO^-$ complex, and 2) O1-N distance to describe the formation of the O-N bond of the heme-bound $[ONO_2]^-$ nitrato-complex. O1 is the O-atom bound to Fe, O2 is the distal O-atom of dioxygen, and N is the nitrogen atom of the •NO substrate. The relevant numbering is depicted in figure 2.1.

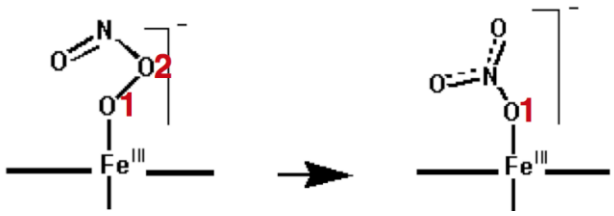

Figure 2.1 Selection of reaction coordinates used to elucidate the peroxynitrite isomerization mechanism. The O1-O2 distance describes the homolytic cleavage of the peroxynitrite O-O bond and the O1-N distance describes the formation of the O-N bond of the heme-bound nitrato complex. The imidazole group coordinating the heme is omitted from the figure.

Geometry optimizations were performed on individual points on the energy grid with the two reaction coordinates fixed at values between 1.25 and 3.75 Å and scanned in 0.25 Å increments. 121 geometry optimizations were performed to complete the 2D PES. The geometries were optimized using the hybrid three parameter Becke-Lee-Yang-Parr (B3LYP) [42] exchange-correlation functional. Unrestricted B3LYP was used given the open-shell nature of the reaction intermediates. Fragment-based geometry optimizations were carried out with 6-311G(d,p) all-electron localized basis sets for C, N, O and H atoms and with LANL2DZ double-ζ basis set with a ten-electron effective core potential (ECP) for Fe. This approach has been recently found to accurately reproduce experimental energy gaps of ground-state spins and low-lying spin-multiplets of penta- and hexa-coordinated iron-prophyrin complexes, to capture the triplet to singlet spin-crossover mechanism for the O_2 binding reaction to penta-coordinated iron-porphyrin-imidazole complex, and to describe the antiferromagnetic nature of the iron-dioxygen chemical bonding [43].

Additional QM(DFT) geometry optimizations were carried out to investigate the NOD product dissociation in gas phase. To obtain the dissociation energy profile for nitrate, geometry optimizations were performed with the Fe-N reaction coordinate scanned from 2.75 to 6 Å, in 0.25 Å increments. The optimized structure of nitrate-bound to the iron-porphyrin-imidazole complex – the global minimum on the 2D PES for peroxynitrite isomerization reaction – was used as a starting point for the nitrate dissociation calculations.

2.2 NOD reaction in trHbN environment

Hybrid QM(DFT)/MM MD simulations were carried out in order to elucidate the NOD reaction mechanism in the enzyme environment and to determine the influence of trHbN active site residues on catalysis. The QM(DFT) approach is required to model a chemical reaction as it provides an accurate description of the electronic structure of an enzyme active site at a moderate computational cost relative to *ab initio* calculations. Nonetheless, QM(DFT) is far too expensive to model the whole system. Molecular mechanics (MM) is thus used to model the enzyme and surrounding solvent using the classical framework in which atoms are treated as point charges and all-atoms interactions (force) are modeled using the first derivative of a simple potential energy function with respect to atomic coordinates – an empirical force field (FF). Hybrid QM/MM computations thus combine the accuracy of all-electron wavefunction model for the QM subsystem undergoing a chemical reaction (QM reactive region) with the computational efficiency of empirical FFs methods, which provide a good description of the electrostatic and steric effects of the surrounding protein on reactivity. The coupling between the two regions describes

the polarization of the QM electron density by MM point charges and can be specified using, for instance, a link atom approach [44]. Furthermore, hybrid QM/MM MD simulations allow for free energy calculations of large enzymatic systems (by opposition to their static (non-MD) QM/MM calculations). Free energy or potential of mean force (PMF) corresponds to the thermodynamic work required to drive chemical reactions along constrained reaction coordinates in the protein environment, giving information about both the rate and the mechanism by which they occur. Constrained QM/MM MD simulations incorporate the effects of thermal fluctuations and the rearrangement of protein residues in the active site of an enzyme during catalysis.

All QM/MM computations were performed with the open-source CP2K molecular simulation package [45]. QM(DFT) calculations, for treatment of the trHbN catalytic site using generalized gradient approximation Becke-Lee-Parr (BLYP) density functional, were performed using the QuickStep density functional module [46] of CP2K. Goedecker-Tetter-Hutter (GTH) pseudopotentials and DZVP-MOLOPT-SR-GTH short-range basis sets optimized for molecular systems [47] were used for all atoms to reduce computational cost. FIST module [45] of CP2K with CHARMM27 force field [48] parameterization was used to calculate the interaction energy of the classical MM subsystem. The Integrated Molecular Orbital Molecular Mechanics (IMOMM) link atom approach [44] was used to treat the covalent bonds across the QM/MM boundary. In this approach an additional QM hydrogen atom is placed along the bonds between the frontier QM and MM atoms to satisfy valence. The electrostatic coupling between MM charges and the QM density represented as point charges was calculated by a linear-scaling real space multi-grid procedure [49], implemented in the CP2K code. QM/MM MD simulations were performed at constant temperature (T = 298.15 K).

The QM subsystem in the QM/MM simulations included the iron-porphyrin ring, the dioxygen ligand, the •NO substrate, and the side-chains of trHbN active site highly-conserved residues: the proximal His81(F8), and distal Tyr(33)B10, Gln58(E11) and Phe46(CD1). The surroundings (i.e. rest of the protein, TIP3P water molecules, counter-ions to balance the protein charges and a few •NO molecules in solution) were treated classically. Link atoms were used in the heme and in the proximal and distal residues to separate the porphyrin ring from the heme substituents (i.e. propionates, vinyl and methyl groups; C-C truncations) and the side-chains of active site residues from the peptidic backbone (i.e. C_α-C_β truncations; C_α MM kind and C_β QM kind). The final system consisted of 96 QM atoms and 36118 MM atoms.

Several replicas of unconstrained QM/MM MD simulations at least 10 ps each of oxy-trHbN with •NO in the active site were conducted using selected snapshots from classical MD simulations [23] as the initial structure. Unconstrained simulations were carried out to observe if the NOD isomerization reaction happens spontaneously in trHbN environment.

Constrained simulations were performed to fully elucidate the NOD reaction mechanism in trHbN environment and to understand the role of trHbN active site residues in assisting the reaction. Unlike unconstrained simulations, in constrained simulations the reaction is driven along representative reaction coordinates maintained fixed by the application of constraint forces. The single-sweep method for free energy calculations [50] was employed to build a two-dimensional PMF for the NOD isomerization reaction. Briefly, in the single-sweep method, the free energy is represented as a summation of Gaussian radial-basis functions at centers (i.e. sampling windows) where constraint forces are simulated. The free energy is dependent on adjustable parameters, including the height and the width (σ) of the Gaussian function. The reconstruction of the PMF consists of finding the N heights and the value of σ that give the mean forces that best model the simulated ones at the centers (N represents the number of centers). Using a linear algebraic system, a PMF solution is found by minimizing an objective error function that measures the discrepancy between the negative gradient of the free energy (i.e. mean forces for the PMF) and the constrained forces obtained from the simulations (i.e. opposite of the estimated mean forces) over the parameters (e.g. σ) until optimal ones are reached.

The PMF for the NOD isomerization reaction was reconstructed from average constraint forces extracted from Lagrange multipliers computed by individual simulations carried out with O1-O2 and O1-N reaction coordinates constrained and the rest of the system free to move. A total of 99 constrained simulations, 10 ps each, were carried out to build the PMF for the NOD isomerization reaction. The average constrained forces where calculated using only the last 9 ps from each simulation. The first 1 ps of equilibration was discarded from the average calculations. The reaction coordinates chosen for the construction of the PMF are the same as those selected for gas-phase calculations of the NOD reaction and were described in section 2.1. Snapshots from trajectories generated by completed and adjacent QM/MM constrained simulations were used as starting structures for all sampling windows on the free energy landscape, except for the first window where a snapshot from unconstrained simulations was used as initial structure.

Constrained QM/MM MD simulations were also performed to understand what prevents the oxidation and nitration of Tyr33(B10) residue and the permanent degradation of trHbN itself.

Constrained QM/MM MD simulations were conducted to investigate the dissociation and release of the product of the NOD reaction in trHbN environment and to understand the role of Tyr33(B10)/Gln58(E11) pair and also Phe46(CD1) and Phe32(B9) active site residues in promoting nitrate dissociation and release. A total of 14 constrained simulations, 10 ps each, were carried out to build a one-dimensional PMF for the NOD nitrate anion release. The optimized structure of heme-bound nitrato-complex – the global minimum on the 2D PMF of the peroxynitrite isomerization reaction – was used as a starting point for the nitrate release simulations. The protocol for conducting the constrained simulations for product release in selected sampling windows is identical to that followed in the case of the NOD isomerization reaction described above. Similarly to the gas-phase calculations, the Fe-N distance was chosen as a reaction coordinate to describe the dissociation of the nitrate anion from the ferric heme iron. The simulations were carried out in sampling windows with the Fe-N reaction coordinate constrained at distances in the 2.75 to 6.0 Å range and scanned by increments of 0.25 Å. While the reconstruction of the 2D PMF surface for the NOD isomerization reaction required the more complex single-sweep method for free energy calculations [50], the 1D PMF for product release was constructed by straightforward numerical integration of the average mean forces obtained from the QM/MM MD constrained simulations using the trapezoidal rule.

Chapter 3

NOD Reaction: Heme-catalyzed peroxynitrite isomerization

3.1 Gas-phase model of NOD peroxynitrite isomerization

To investigate the NOD isomerization reaction in gas phase and validate the reaction coordinates chosen to examine the process, a two-dimensional potential energy surface (2D PES) was constructed. Figure 3.1 shows the resulting 2D PES of the NOD isomerization reaction as a function of the O1-O2 and O1-N reaction coordinates. The points on the potential energy grid, where individual geometry optimizations were performed, are marked as black dots on the 2D PES. The full range of possible reactions involving $OONO^-$ and $\bullet NO_2$ intermediates has been captured on the 2D PES. The optimized structures of the NOD isomerization reaction intermediates, $OONO^-$, compound II and $\bullet NO_2$, and bound nitrate are mapped and indicated by red arrows on the 2D PES.

Mechanism.

The gas-phase results suggest that the $OONO^-$ isomerization proceeds in a *sequential* manner. Following $OONO^-$ formation from the attack of free •NO on coordinated superoxide, the peroxo O1-O2 bond undergoes homolysis to give a very stable oxo-ferryl species (Fe^{IV}=O), as evidenced by a short Fe-O1 bond distance (Table 3.1), and an $\bullet NO_2$ radical. The $\bullet NO_2$ intermediate then turns around (Figure 3.2 C) and its nitrogen attacks the oxo-ferryl, forming the O1-N bond and nitrate bound to ferric iron – the most stable, energetically favorable structure on the 2D PES. Thus, the isomerization reaction proceeds sequentially along the minimum energy path from bound $OONO^-$ (calculated at the grid point where O1-O2 and O1-N reaction coordinates were fixed at 1.50 and 2.50 Å, respectively), to oxo-ferryl (Fe^{IV}=O1) species and free $\bullet NO_2$ radical (at 3.25 Å O1-O2 and 3.00 Å O1-N distances), and ending at the overall global minimum corresponding to bound-NO_3^- (calculated at an O1-O2 distance of 2.25 Å and an O1-N distance of 1.50 Å).

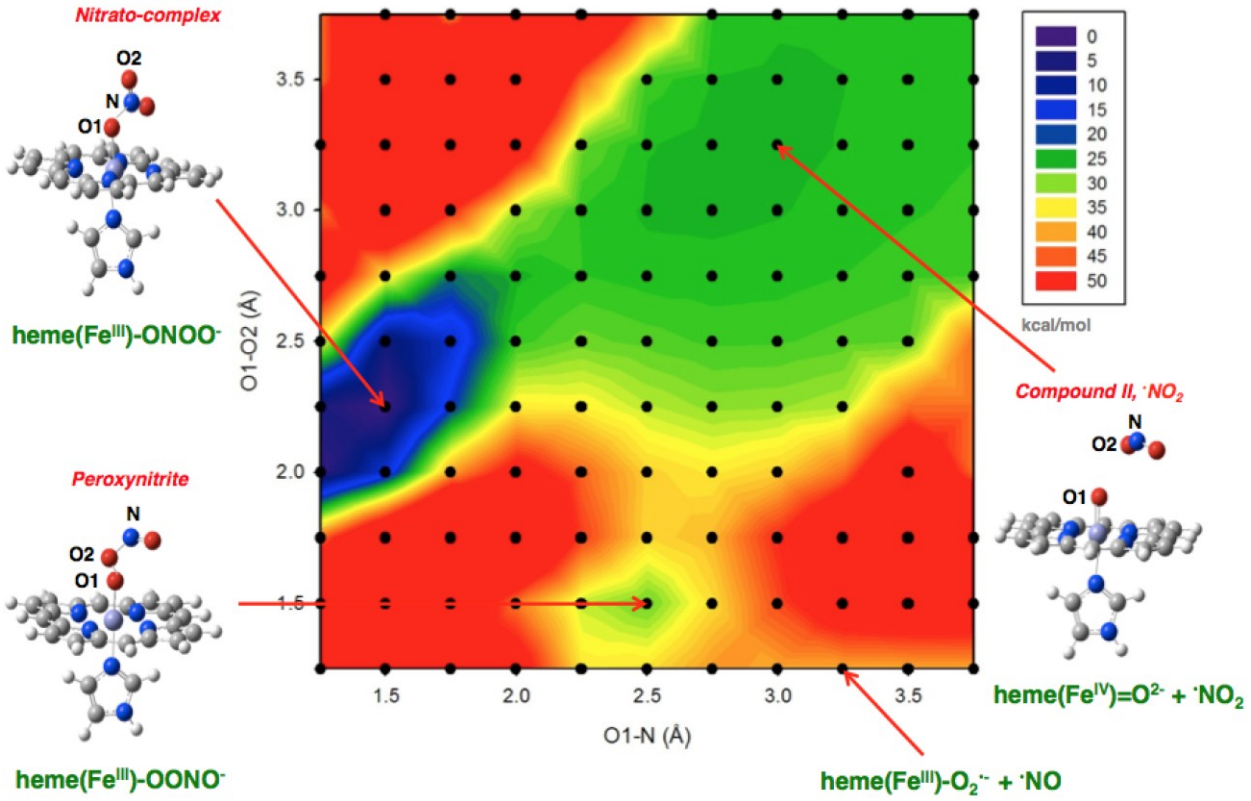

Figure 3.1 Two-dimensional potential energy surface (2D PES) of the NOD isomerization reaction in gas phase. The grid points where individual geometry optimizations were performed at UB3LYP/6-311G(d,p) with ECP/LANL2DZ for Fe level of theory are marked as black dots. The optimized structures of the NOD isomerization reaction intermediates and bound nitrate are mapped and indicated by red arrows on the 2D PES. The energy surface suggests a highly exergonic sequential mechanism involving rapid formation of peroxynitrite, followed by formation of the •NO_2 radical intermediate, and by formation of heme-bound nitrate.

Structures of the intermediate species involved in isomerization reaction.

The optimized geometries of the complexes captured on the 2D PES of the NOD isomerization reaction are given in Table 3.1. The geometries obtained with UB3LYP/6-311G(d,p) with ECP/LANL2DZ for Fe are in excellent agreement with previous results from electronic structure calculations performed at B3LYP/6-31G** level of Mishra et al [33]. For instance, for the bound $OONO^-$ complex, the O2-N distance is 1.41 Å and Fe-O1 is 1.81 Å in both works, N-O distance is 1.17 Å (1.18 Å [33]), Fe-O1-O2 bond angle is 113.2° (114° [33]), and the O-N-O1-O2 dihedral angle is 177.3° (177.4° [33]). Noteworthy are the geometrical parameters for the compound II and dissociated •NO_2 complex. The Fe-O1 bond

distance is 1.62 Å in both works. The short Fe-O1 bond distance of double-bond character provides evidence for oxo-ferryl species (Fe^{IV}=O1). Similarly, O2-N and O-N bond lengths are equal with a value of 1.19 Å (1.23 Å [33]), and O2-N-O angle is 134° in both works, providing strong evidence for •NO_2 radical formation (and not nitrite, NO_2^-).

Table 3.1 Relevant geometrical parameters for the intermediates of the NOD isomerization reaction.

	$Fe^{III}[^-OONO]$ →	Fe^{IV}=O + •NO_2 →	$Fe^{III}[^-ONO_2]$
O1 – O2	1.50 (1.425)	3.25	2.25 (2.227)
O1 – N	2.50 (2.315)	3.00	1.50 (1.346)
O2 – N	1.419 (1.416)	1.913 (1.231)	1.201 (1.224)
N – O	1.172 (1.188)	1.913 (1.231)	1.204 (1.227)
Fe – O1	1.817 (1.81)	1.624 (1.622)	1.852 (1.88)
Fe – O1 – O2	113.2 (114)		
O2 – N – O	117.2 (109)	134.2 (134)	128.8 (125)
O – N – O2 – O1	177.3 (177.4)		178.1 (180)

Bond lengths (Å) and bond angles (degrees) obtained with UB3LYP/6-311G(d,p) with ECP/LANL2DZ for Fe. Values in parenthesis correspond to the parameters obtained with B3LYP/6-31G** by Mishra et al [33].

Energetics for the isomerization of peroxynitrite to bound nitrate in gas phase.

In gas phase, $OONO^-$ isomerization occurs sequentially with *short-lived* intermediates. As the energy profile in figure 3.2 B shows, formation of oxo-ferryl species and •NO_2 radical by homolysis of peroxynitrite O1-O2 bond is energetically favored by 3.4 kcal/mol. The energy profile shows a rather large (7.8 kcal/mol) activation barrier for the homolytic cleavage of the peroxo bond, which would indicate that homolysis occurs on sub-microsecond timescale, thus making O1-O2 bond scission the rate-limiting step in the NOD isomerization reaction. Nonetheless, the transition state was just estimated from the 2D PES of the isomerization reaction. On the other hand, rebinding of •NO_2 to compound II is almost

barrierless (1.2 kcal/mol) and extremely fast (picosecond timescale). The results indicate that the oxo-ferryl species and $\bullet NO_2$ radical intermediates of the NOD isomerization reaction are extremely short-lived. The overall isomerization reaction is exergonic by 28.2 kcal/mol (supporting the sequential mechanism).

The same energy profile calculated with BLYP density functional compares well with the B3LYP profile shown in figure 3.2 B. With BLYP, the overall sequential isomerization reaction is exergonic by 22.2 kcal/mol. The activation barrier for the homolysis elementary step is 7 kcal/mol lower compared to the B3LYP calculations (0.8 kcal/mol). Formation of oxo-ferryl species and $\bullet NO_2$ radical is energetically favored by 7.4 kcal/mol. The activation barrier for $\bullet NO_2$ rebinding is larger by 3 kcal/mol and the state is energetically favored by 3.2 kcal/mol relative to peroxynitrite. In the trHbN environment, the barrier is lowered to the B3LYP level due to favorable interactions assisting the $\bullet NO_2$ rebinding elementary step (see section 3.2).

A high-energy barrier of approximately 30 kcal/mol, between the peroxynitrite-complex and the nitrato-complex on the 2D PES, does not support the *concerted* rearrangement mechanism – the diagonal path from $OONO^-$ to bound-nitrate on which O1-O2 reaction coordinate increases and O1-N reaction coordinate decreases – for the peroxynitrite isomerization in gas phase. Similarly, Blomberg et al [31] in their models of the NOD reaction in Mb employing hybrid DFT reportedly failed to find a concerted mechanism yielding plausible activation energies, supporting instead the oxo-ferryl (i.e. sequential) mechanism given an energy barrier for the O-O bond homolysis of ~10 kcal/mol and a highly exergonic overall reaction sequence (29 kcal/mol). In addition, hybrid DFT analysis of models of trHbN NOD reaction by Crespo et al [32] suggested a similar highly exergonic sequential mechanism (28 kcal/mol).

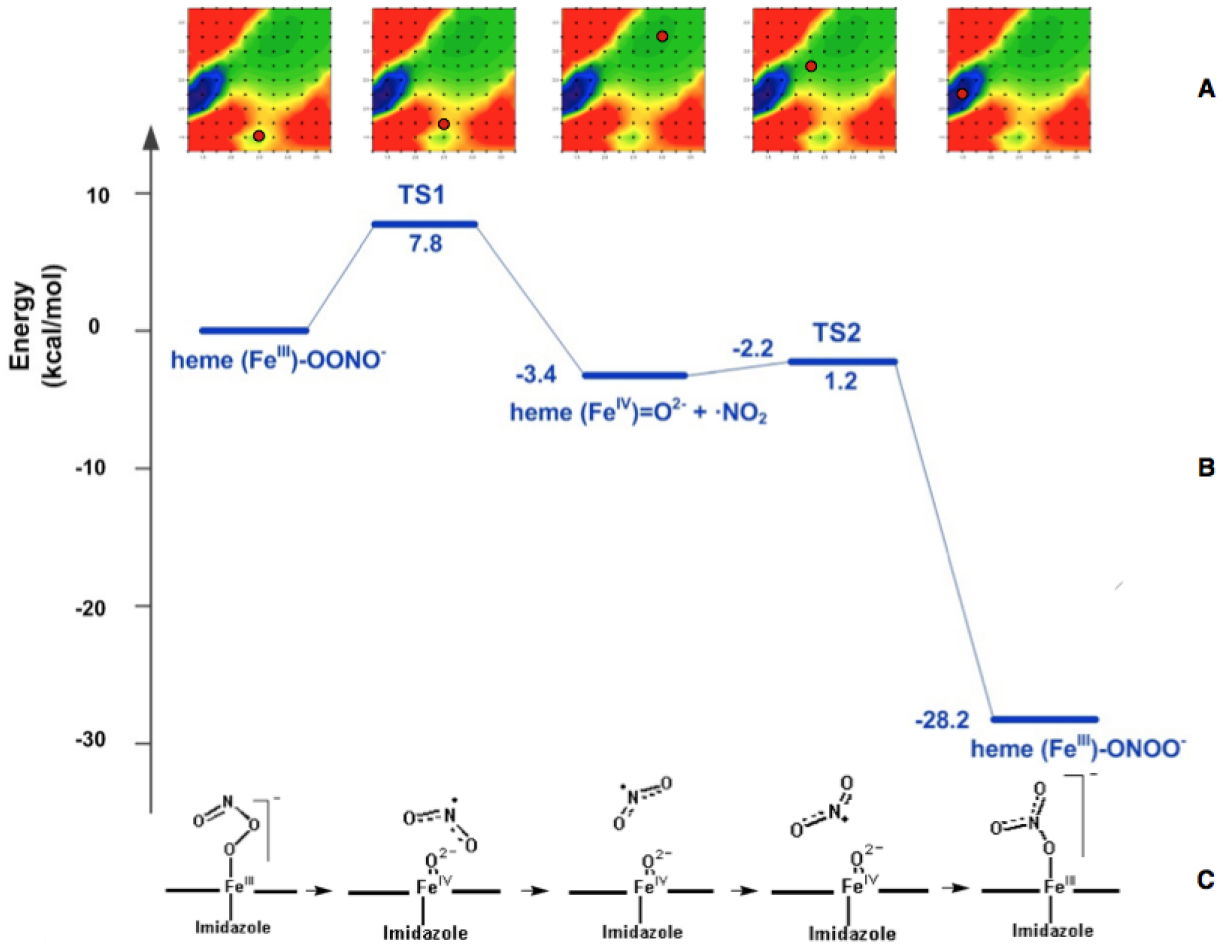

Figure 3.2 Energy profile of the trHbN NOD isomerization reaction in gas phase. (A) Red dots on the 2D PES mark the positions of the grid points at which the potential energy of each state (i.e. intermediates, transition states and bound product) is calculated. (B) Potential energy differences and activation barriers for the complexes in A relative to that of peroxynitrite. The energy profile suggests a highly exergonic sequential mechanism with very short-lived intermediates. (C) Schematic of the isomerization reaction illustrating formation of oxo-ferryl species and •NO_2 radical intermediates, the •NO_2 radical rotation and its rapid rebinding to oxo-ferryl species to form bound nitrate. See text for more details.

3.2 NOD peroxynitrite isomerization in trHbN environment

To fully elucidate the NOD isomerization reaction by incorporating the effects of thermal fluctuations and the rearrangement of trHbN residues at the active site, both unconstrained and constrained QM(DFT)/MM MD simulations were performed in trHbN environment.

Mechanism.

Our unconstrained simulations of oxy-trHbN with •NO in the active site show that the NOD isomerization reaction occurs spontaneously in a *sequential* manner. Peroxynitrite ($OONO^-$) forms within 1 ps of simulation time, and its isomerization to stable oxo-ferryl (Fe^{IV}=O) species and dissociated •NO_2 follows rapidly in about 2.5 ps.

A two-dimensional potential of mean force (PMF) was reconstructed from mean forces obtained from constrained QM/MM simulations using the same reaction coordinates as those used in gas-phase calculations. Constraints were imposed on O1-O2 and O1-N reaction coordinates to drive the isomerization reaction in trHbN environment. The rest of the system was let free to undergo thermal fluctuations. Figure 3.3 shows the resulting 2D PMF. Sampling windows where individual 10 ps constrained simulations with fixed reaction coordinates were performed are marked as black dots on the 2D PMF. Schematic representations of the active site including reaction intermediates and bound product, as observed from our constrained simulations, are mapped along the minimum free energy reaction path on the PMF (red arrows).

The 2D PMF confirms the *sequential* mechanism of the NOD heme-catalyzed $OONO^-$ isomerization reaction – the minimum free energy reaction path starting with $OONO^-$ formation from free •NO attack on the ferric superoxide complex at O1-O2 and O1-N distances of 1.50 and 2.50 Å, respectively, followed by $OONO^-$ O1-O2 peroxo bond homolytic cleavage and formation of stable oxo-ferryl (Fe^{IV}=O1) species and free •NO_2 radical at O1-O2 and O1-N distances of 3.25 Å and 3.00 Å, respectively, and ending at the overall global minimum corresponding to bound-nitrate, obtained from the simulation window where O1-O2 and O1-N distances were constrained at 2.25 Å and 1.50 Å, respectively.

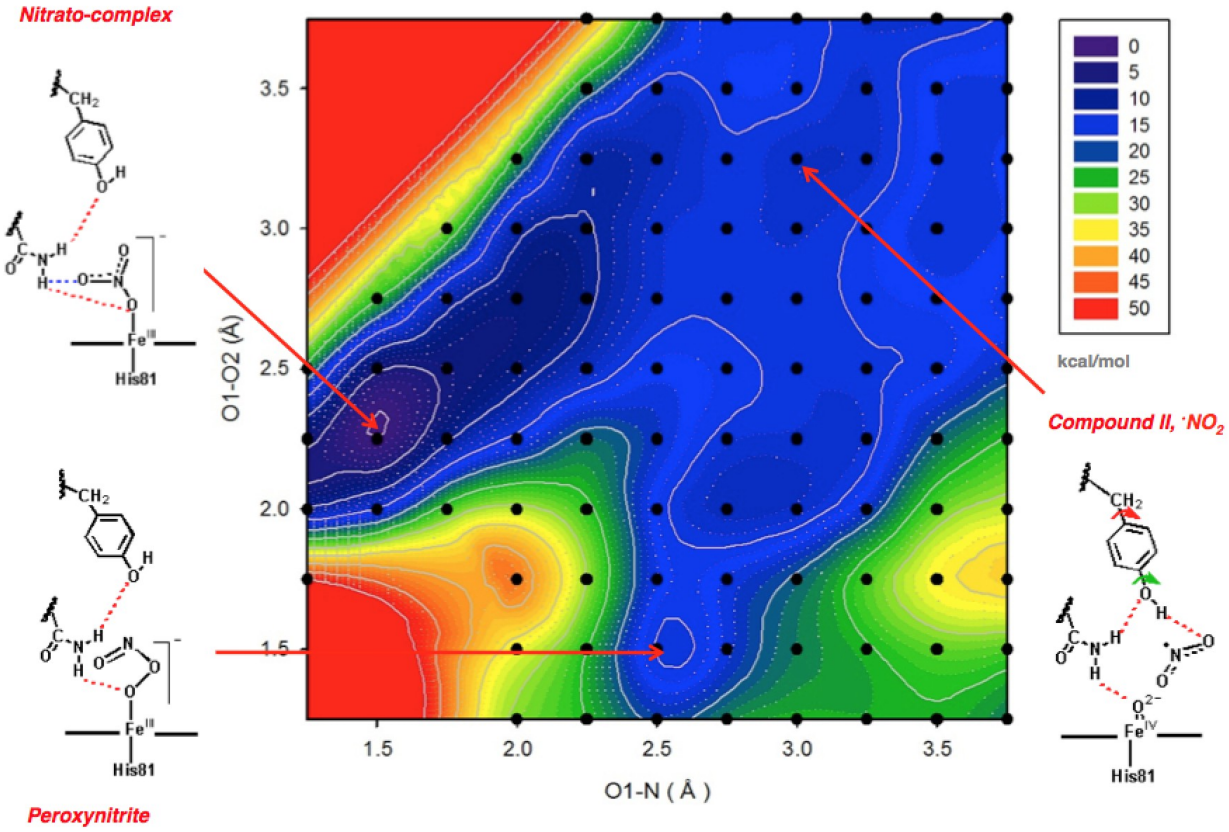

Figure 3.3 Two-dimensional potential of mean force (2D PMF) of the NOD isomerization reaction in trHbN environment. The sampling windows where individual 10 ps constrained QM/MM MD simulations with fixed O1-O2 and O1-N reaction coordinates were performed are marked as black dots on the 2D PMF. Schematic representations of the trHbN active site including reaction intermediates and bound product, as observed from our constrained simulations, are mapped along the minimum free energy reaction path on the 2D PMF and indicated with red arrows. The free energy surface suggests a highly exergonic and extremely fast sequential mechanism involving rapid formation of peroxynitrite, followed by its rapid homolysis to oxo-ferryl species and •NO_2 radical intermediates, and by fast formation of heme-bound nitrate.

Figure 3.4 shows a detailed schematic of the sequential mechanism as observed from analysis of trajectories obtained from 5 sampling windows (9 ps for each window). It includes the 3 minima mentioned above as well as the transition states for the stepwise isomerization mechanism (the transition states energies are estimated from the PMF). Following $OONO^-$ homolysis, $\bullet NO_2$ rotates and it is properly positioned to attack the oxo-ferryl heme in a rebound type of mechanism and form the O1-N bond of the NO_3^- product bound to ferric iron. The *concerted* mechanism, the diagonal path from $OONO^-$ to bound-nitrate on which O1-O2 reaction coordinate increases and O1-N reaction coordinate decreases, can be ruled out due to the large, > 30 kcal/mol, free energy barrier.

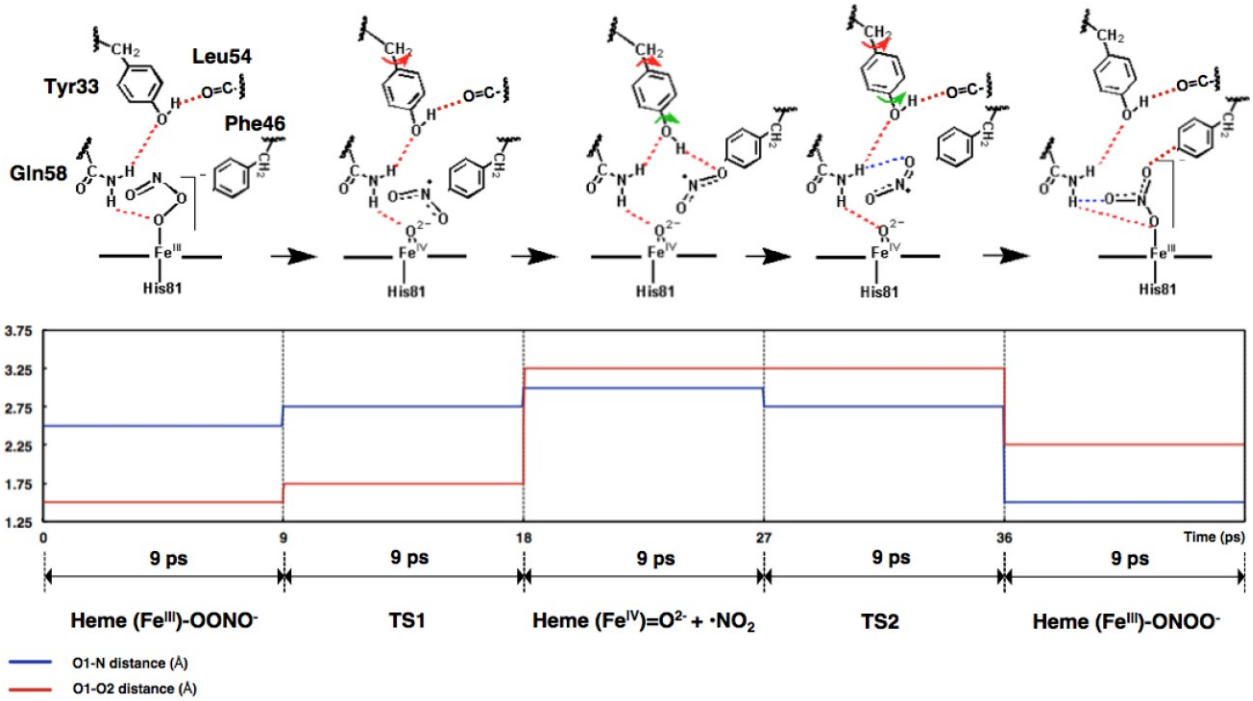

Figure 3.4 Schematic of the sequential mechanism based on analysis of trajectories obtained from constrained QM/MM MD simulations (*Top*). The dashed lines and arrows shown in the schematic are explained in the trHbN dynamics subsection of the text. (*Bottom*) Constraints imposed on O1-O2 (red) and O1-N (blue) reaction coordinates in five individual simulations from which the three minima and transition states were obtained. Black dashed lines delimit the simulation windows, 9 picoseconds each.

Energetics for the isomerization of peroxynitrite to bound nitrate in trHbN environment.

Heme-catalyzed $OONO^-$ isomerization occurs sequentially with very *short-lived* intermediates. As shown in figure 3.5 B, formation of oxo-ferryl species and $\bullet NO_2$ radical from peroxynitrite O1-O2 bond homolytic fission is energetically favored by 1.6 kcal/mol with a low activation barrier of 2.4 kcal/mol.

Rebinding of $\bullet NO_2$ to compound II is almost barrierless (1.5 kcal/mol), and the overall isomerization reaction in trHbN environment is exergonic by 14.7 kcal/mol. These energetics show that $OONO^-$ isomerization to bound-nitrate occurs on picoseconds timescale and is not the rate-limiting step in the overall rapid NOD reaction.

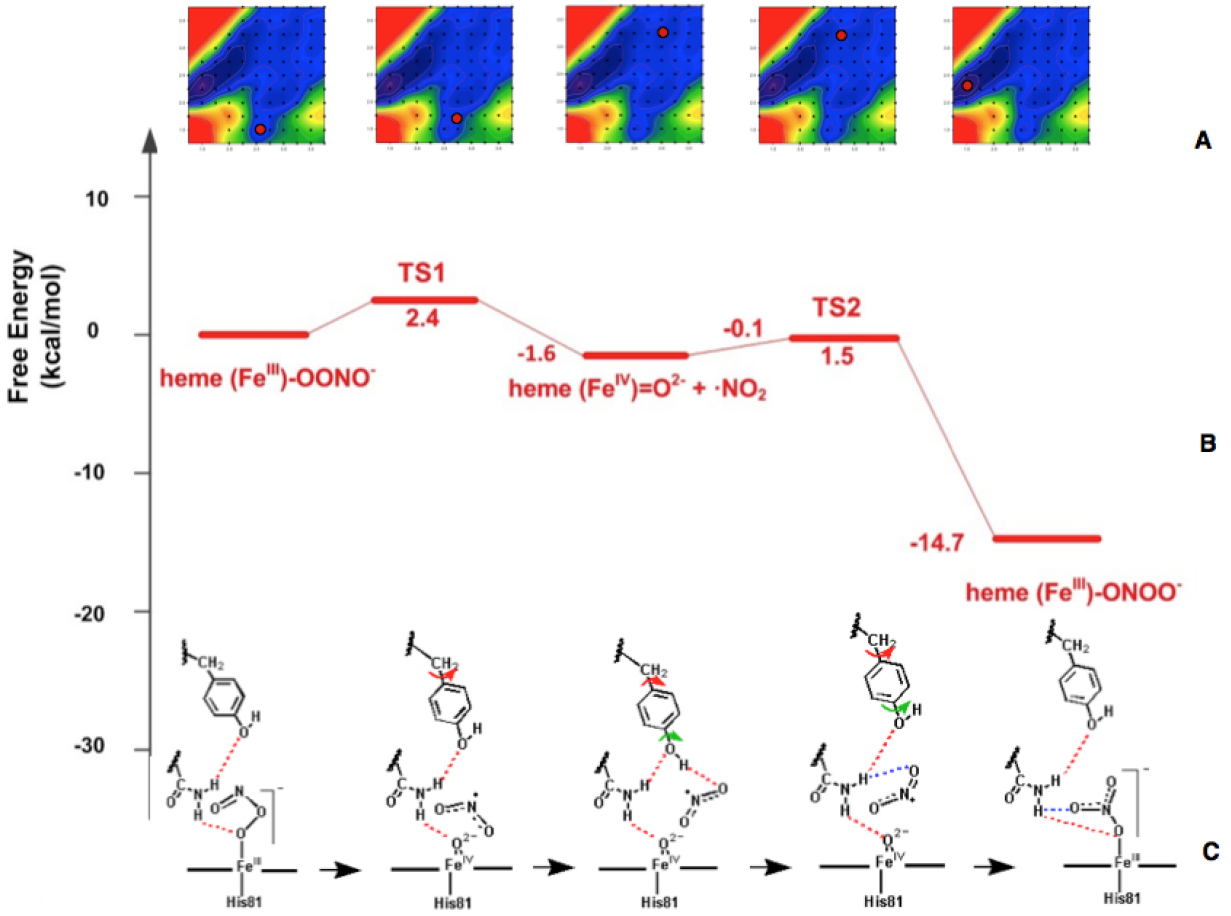

Figure 3.5 Free energy profile of the trHbN NOD isomerization reaction in trHbN environment. (A) Red dots on the 2D PMF mark the positions of the simulation windows at which the free energy of each state (i.e. intermediates, transition states and bound product) is computed. (B) Free energy differences and activation barriers relative to that of peroxynitrite. The free energy profile suggests a highly exergonic sequential mechanism with very short-lived intermediates. The energetics show that $OONO^-$ isomerization to bound-nitrate occurs on picoseconds timescale and is not the rate-limiting step in the overall rapid NOD reaction. (C) Schematic of the sequential mechanism as observed from constrained QM/MM MD simulations. See trHbN dynamics subsection of the text for details.

TrHbN dynamics during the heme-catalyzed peroxynitrite isomerization to bound nitrate.

Gardner et al studies [17] on the NOD reaction in *E. coli* flavoHb have shown that its active site residues, Leu(E11), Val(G8), Phe(CD1), Phe(B9) and Tyr(B10), sterically and electrostatically facilitate and cage the NOD isomerization reaction. Given the high similarity between flavoHb and trHbN active sites, Crespo et al [32] hypothesized that the •NO reaction with Fe^{III}-$O_2^{\bullet-}$ and the isomerization reaction in trHbN of Mtb occur in the distal cavity formed by the highly conserved residues: Gln58(E11), Val94(G8), Phe46(CD1), Phe32(B9) and Tyr33(B10) which may trap the isomerization intermediates. In this work, we show not only that trHbN distal heme pocket residues isolate the isomerization intermediates but also that concerted motions of Tyr33(B10), Gln58(E11), Phe46(CD1), Phe32(B9), and Val94(G8) assist the fast reaction of the transient •NO_2 with oxo-ferryl species to form the heme-bound nitrato-complex.

Analysis of trajectories obtained from our simulations show that *Tyr33(B10) is involved in a dynamic hydrogen-bonding network with both Gln58(E11) and Leu54(E7)*. As illustrated in figure 3.6, Tyr33(B10) O atom of the phenol group acts as a H-bond acceptor of the Gln58(E11) amide N atom, while Tyr33(B10) in a H-bond donor to the O atom of the backbone carbonyl group of *Leu54(E7)*. The H-bond between Tyr33(B10) and Gln58(E11) is very stable and maintained throughout the entire isomerization reaction with an average Tyr33(B10):OH–Gln58(E11):HE22 distance of 2.16 Å. The H-bond formed between Tyr33(B10) hydroxyl H atom and the carbonyl O atom of Leu54(E7) backbone is also very stable throughout the reaction. Nonetheless, the Tyr33(B10):HH–Leu54(E7):O H-bond is transiently lost (for more than 1 ps) in the simulation window corresponding to dissociated •NO_2 radical and stable oxo-ferryl species. In this window, at O1-O2 and O1-N distances of 3.25 Å and 3.00 Å, respectively, •NO_2 radical is relatively far from the O-atom (O1) bound to oxo-ferryl species and ascended in the active site. During the same time, *Tyr33(B10) strongly H-bonds the •NO_2 radical*, stabilizing it. The average Tyr33(B10):HH–•NO_2:O distance in this case is 2.50 Å, compared to 6.00 Å average in the simulation where peroxynitrite forms, for instance. The Tyr33(B10)–•NO_2 H-bond is broken in the transition state from •NO_2 and oxo-ferryl species toward bound-nitrate. It appears that it is the breaking of this H-bond that drives the complete rotation of •NO_2 radical. At this stage, •NO_2 radical is properly positioned to descend and attack compound II, having the N atom oriented toward the O atom (O1) bound to the oxo-ferryl species, a position suitable for the formation of the O1-N bond of the bound-nitrate (and not a fall back toward an O-O peroxo bond formation).

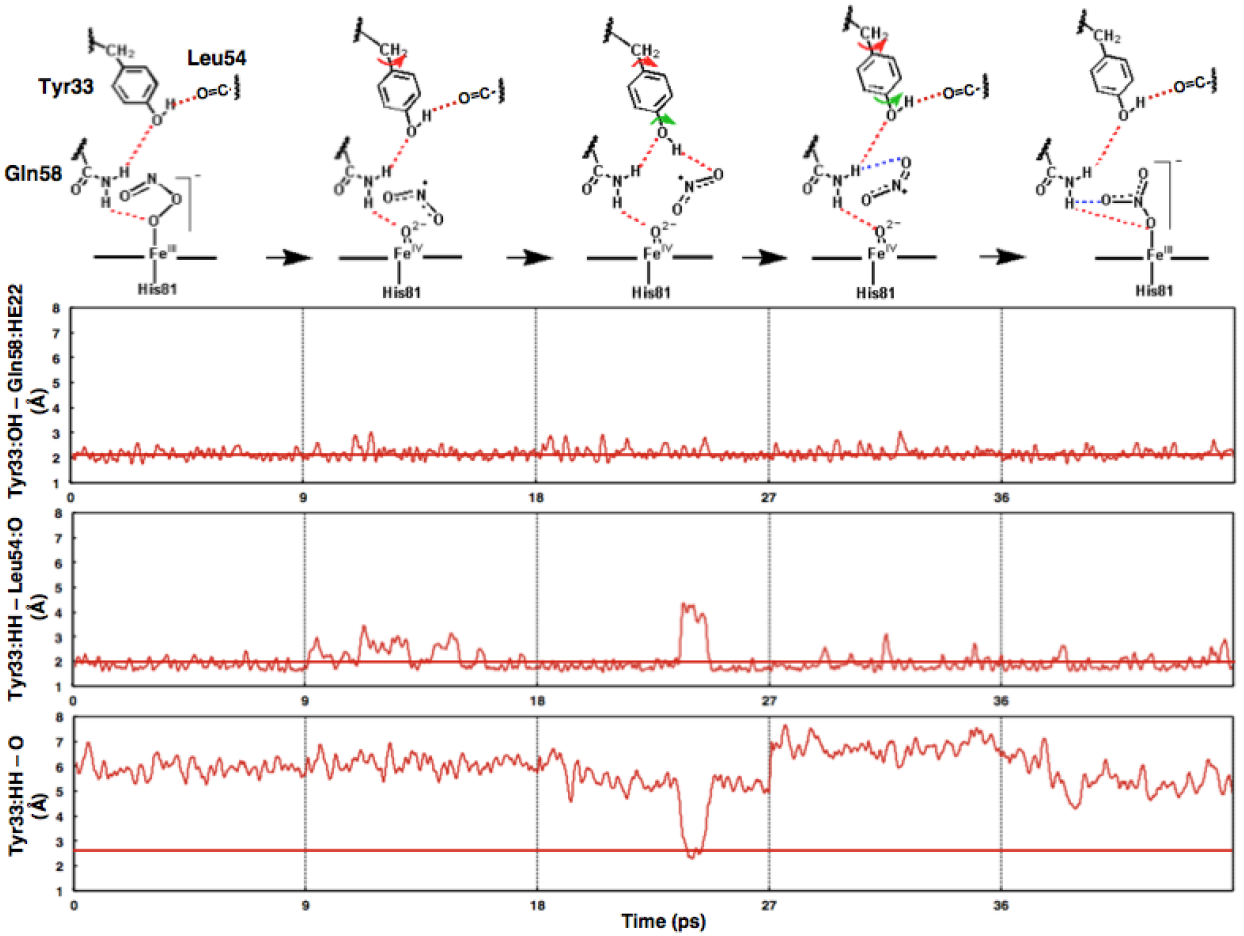

Figure 3.6 Dynamics of the hydrogen-bonding network between Tyr33(B10), distal Gln58(E11) and Leu54(E7) residues, and the •NO_2 intermediate. Tyr33(B10) is H-bonded to Gln58(E11) and Leu54(E7) throughout the entire isomerization reaction. Tyr33(B10) transiently forms a stable H-bond with the •NO_2 radical. Loss of this H-bond drives the rotation and properly orients the •NO_2 radical for the formation of bound-nitrate. See text for details. The hydrogen bonds formed by Tyr33(B10) are identified as red dashed lines on the top schematics. Continuous horizontal red lines indicate stabilizing hydrogen bonding distances.

Tyr33(B10) changes conformation during the isomerization reaction. Analysis of trajectories obtained from our simulations show that Tyr33(B10) changes conformations during the NOD reaction. Two Tyr33(B10) flips are of particular interest here (Figure 3.7). In the simulation where •NO_2 and compound II are most stable, both the phenyl and hydroxyl groups of Tyr33(B10) flip. The phenyl group rotates by as much as 110° as shown in the time series of the χ2 (CA-CB-CG-CD1) dihedral angle in figure 3.7 from a typical (standard) ~100° χ2 value (gauche+ rotamer) for side chains with sp^2 hybridized CG atom (Tyr,

Phe) to an unusual (rarely found rotamer) -10° value for the dihedral angle. Concomitantly, the hydroxyl group rotates by as much as ~150° as evidenced by the time series for the HH-OH-CZ-CE2 dihedral angle showing a change from -130° average to +20° in the angle. These flips orient the Tyr33(B10) hydroxyl group inward the active site and cause the formation of the stabilizing H-bond between Tyr33(B10) hydroxyl hydrogen and the $\bullet NO_2$ radical. In the transition state, the phenyl and hydroxyl groups of Tyr33(B10) rotate again in the opposite direction to position the hydroxyl group outward the active site, the predominant Tyr33(B10) orientation observed in most of the simulations along the NOD reaction path. These backward flips cause the strong H-bond between Tyr33(B10):HH and Leu54(E7) backbone carbonyl to reform, and also the transient H-bond between Tyr33(B10) hydroxyl hydrogen and $\bullet NO_2$ to break which promotes $\bullet NO_2$ to turn around for rebinding to oxo-ferryl species.

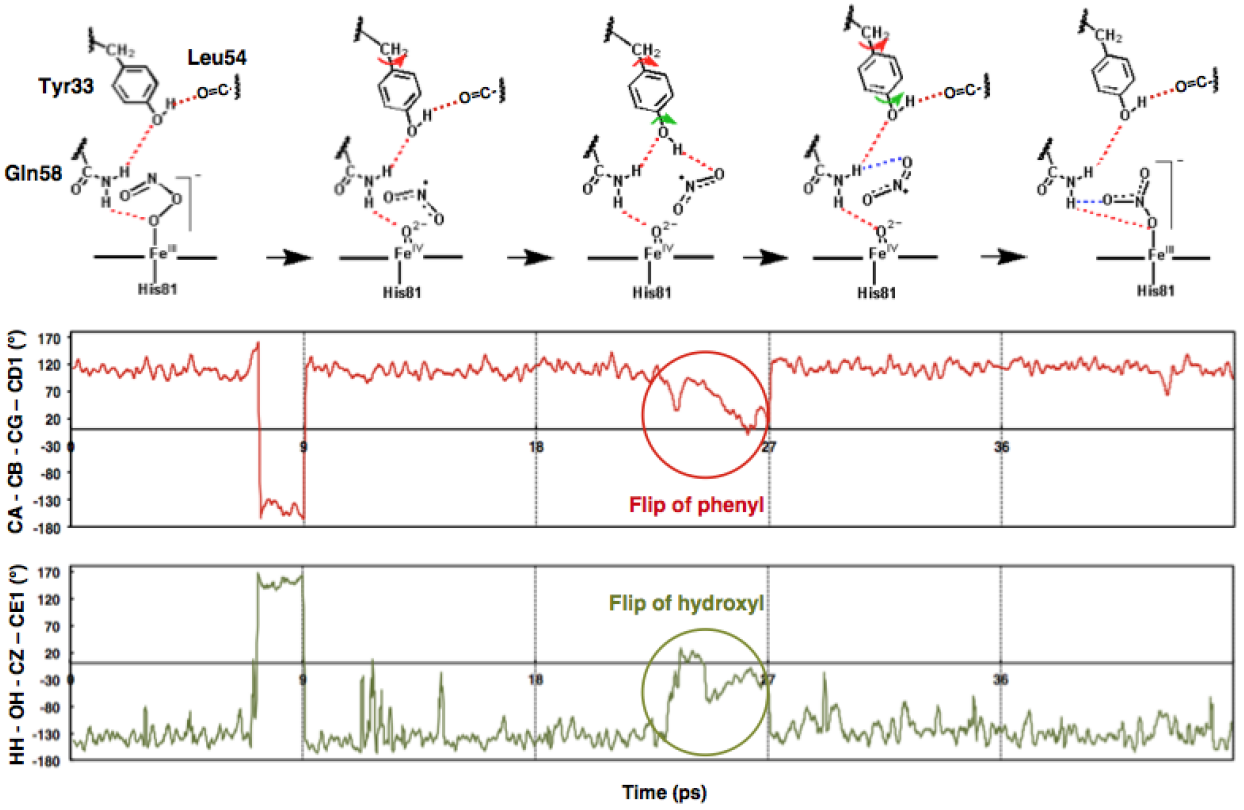

Figure 3.7 Tyr33(B10) conformational changes during the isomerization reaction. Concomitant flips of phenyl and hydroxyl groups cause transient formation and breaking of the H-bond between Tyr33(B10) hydroxyl hydrogen and the $\bullet NO_2$ radical, promoting $\bullet NO_2$ rebinding to oxo-ferryl species. See text for details. The rotations of Tyr33(B10) phenyl and hydroxyl groups are indicated as red and green arrows on the top schematics and as red and green circles in the time series plots for the Tyr33(B10) dihedral angles.

Gln58(E11) stabilizes the O-atom of oxo-ferryl species and assists •NO_2 rebinding via H-bonding. Figure 3.8 shows the overall dynamics of Gln58(E11) interactions with oxo-ferryl species and •NO_2 radical during the NOD isomerization reaction. Our constrained simulations reveal that, in addition to Tyr33(B10), Gln58(E11) plays its own important role in the NOD isomerization reaction. First, it stabilizes the O-atom of oxo-ferryl species and also the O-atom bound to ferric iron of both the peroxynitrite complex and nitrato-complex via H-bonding. The time series for Gln58(E11):HE21–O1 distance (figure 3.8) show an average of 2.45 Å for the stable H-bond maintained during the entire NOD isomerization reaction. Second, it assists •NO_2 rebinding via H-bonding. As mentioned previously, in the transition state from •NO_2 and oxo-ferryl species toward bound-nitrate, •NO_2 radical is properly positioned to attack compound II, (due to the breaking of the transient H-bond between Tyr33(B10) and the •NO_2 radical), having the N atom oriented toward the O atom (O1) bound to the oxo-ferryl species, a position suitable for the formation of the O1-N bond of the bound-nitrate. It is Gln58(E11) that contributes to maintaining this favorable orientation of •NO_2 during its descent from O1-O2 and O1-N distances of 3.25 Å and 3.00 Å, respectively, to an O1-O2 distance of 2.25 Å and an O1-N distance of 1.50 Å where bound nitrate forms. It does so by acting as an amine group H-bond donor to O atoms of the •NO_2 intermediate and bound nitrate. To exemplify, the H-bond length between Gln58(E11):HE22 and •NO_2 intermediate is 2.2 Å minimum, and the H-bond length between Gln58(E11):HE21 and NO_3^- bound product is 2.4 Å minimum (Figure 3.8). Figure 3.8 shows the overall dynamics of Gln58(E11):HE22 and Gln58(E11):HE21–O2 distances during the NOD isomerization reaction.

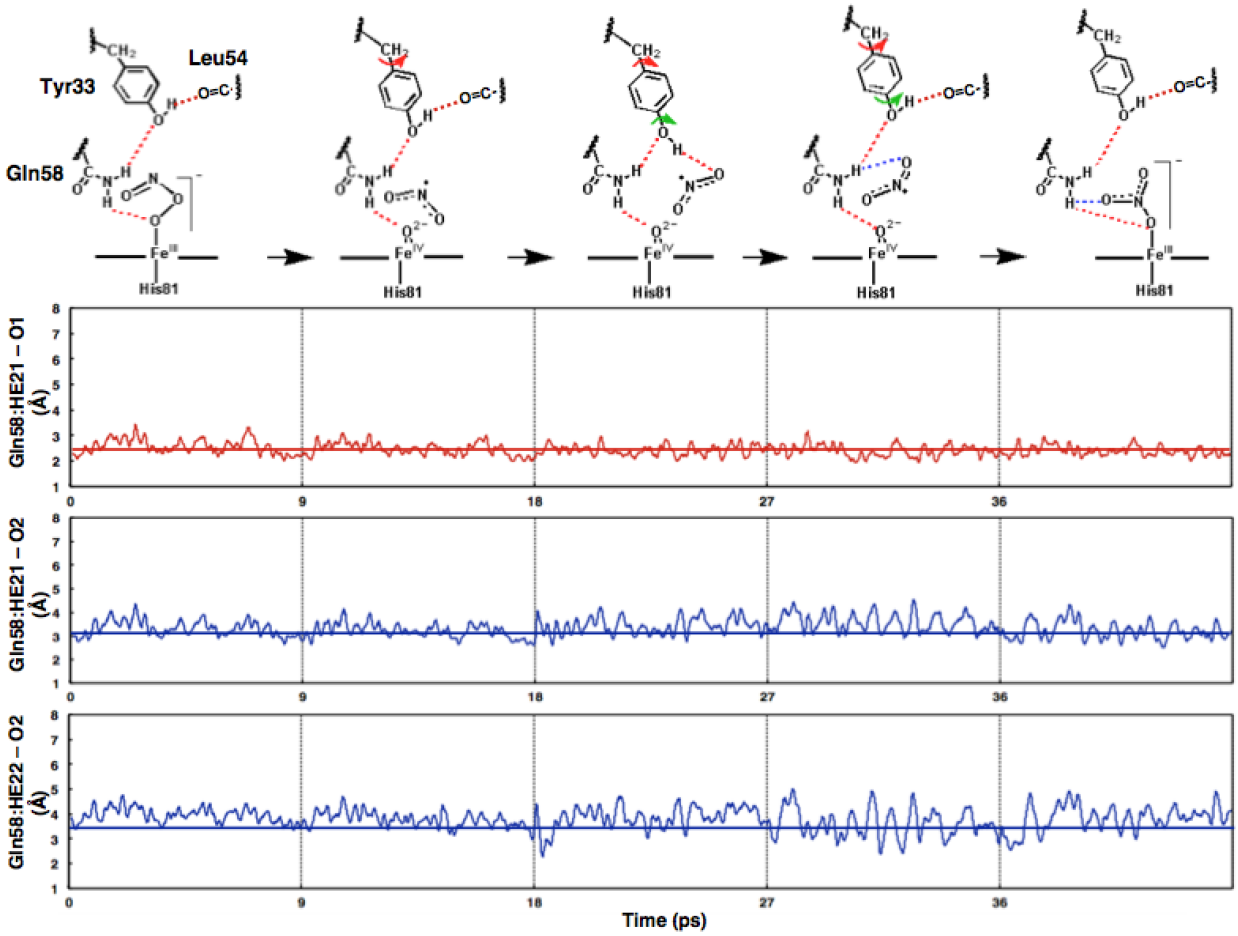

Figure 3.8 Gln58(E11) stabilizes the O-atom of oxo-ferryl species and assists $\bullet NO_2$ rebinding via H-bonding. The hydrogen bonds formed by Gln58(E11) with the O-atom of oxo-ferryl species and the $\bullet NO_2$ radical, stable throughout the entire isomerization reaction, are identified by red and blue dashed lines on the top schematics, respectively.

Phe46(CD1) stabilizes bound NO_3^- to the ferric heme iron via C−H···O hydrogen bonding.

Electronic structure calculations of Bryantsev and Hay [40] showed that benzene forms C−H hydrogen bonds with the nitrate anion that can have as much as 57% of the strength of those formed by O−H group from water, and when present in a receptor (i.e. aromatic side chains in trHbN active site), C−H groups could considerably enhance anion binding affinity [40]. Figure 3.9 shows the optimized geometries and electronic binding energies for the benzene complexes with NO_3^- and the corresponding anion-water complex calculated by Bryantsev and Hay [40] at MP2/aug-cc-pVTZ level of theory. In the global minimum of the benzene NO_3^- complex, two C−H groups contact the anion (Figure 3.9 A). The complex

is asymmetric with one short linear C−H···O bond (H···O distance of 2.20 Å) and one long bent C−H···O bond (H···O distance of 2.40 Å). For the two O−H···O bonds in the H_2O NO_3^- complex (Figure 3.9 C), the corresponding H···O distances are 1.86 and 2.32 Å, respectively. A less stable geometry has also been found by Bryantsev and Hay [40] in which benzene interacts the NO_3^- anion via a single C−H donor (Figure 3.9 B). The binding energy for the global minimum of the benzene NO_3^- complex is -9.26 kcal/mol relative to -16.03 kcal/mol calculated for the water complex showing that the C−H hydrogen bonding interactions between NO_3^- and benzene produce a complex that is 57% as stable as the corresponding water complex [40]. For the less stable geometry, the binding energy of the complex is -7.5 kcal/mol [40]. Our own calculations at B3LYP/6-311G(d,p) level of theory found an optimum geometry comparable with the global minimum of Bryantsev and Hay [40]. The H···O distances of the two C−H···O bonds obtained from our DFT calculations are 2.20 and 2.32 Å, respectively.

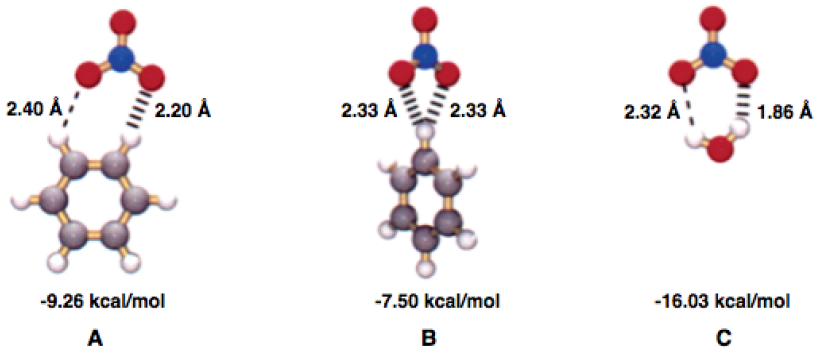

Figure 3.9 Geometries and electronic binding energies for complexes of NO_3^- with benzene (A, B) and water (C) obtained from MP2/aug-cc-pVTZ single-point energy calculations on MP2/aug-cc-pVDZ optimized geometries. C−H···O bonds are indicated with dashed lines. Thinner dashed lines indicate weaker interactions in A and C. Reproduced with permission from Bryantsev, V.S., and Hay, B. P. (2005) J. Am. Chem. Soc. 127 (23), 8282-8283 [40]. Copyright © 2005 American Chemical Society.

The strength of interactions between NO_3^- and benzene suggests that the aromatic side chains of trHbN active site could stabilize the bound NO_3^-, at C−H···O distances comparable to those obtained from electronic structure calculations. The time series in figure 3.10 show, in the simulation window where the bound- NO_3^- product forms, a sharp drop in the Phe46(CD1):HZ–O distance from 5.06 Å to 1.94 Å. At this distance, Phe46(CD1) stabilizes NO_3^- bound to the ferric heme iron by C−H···O hydrogen bonding.

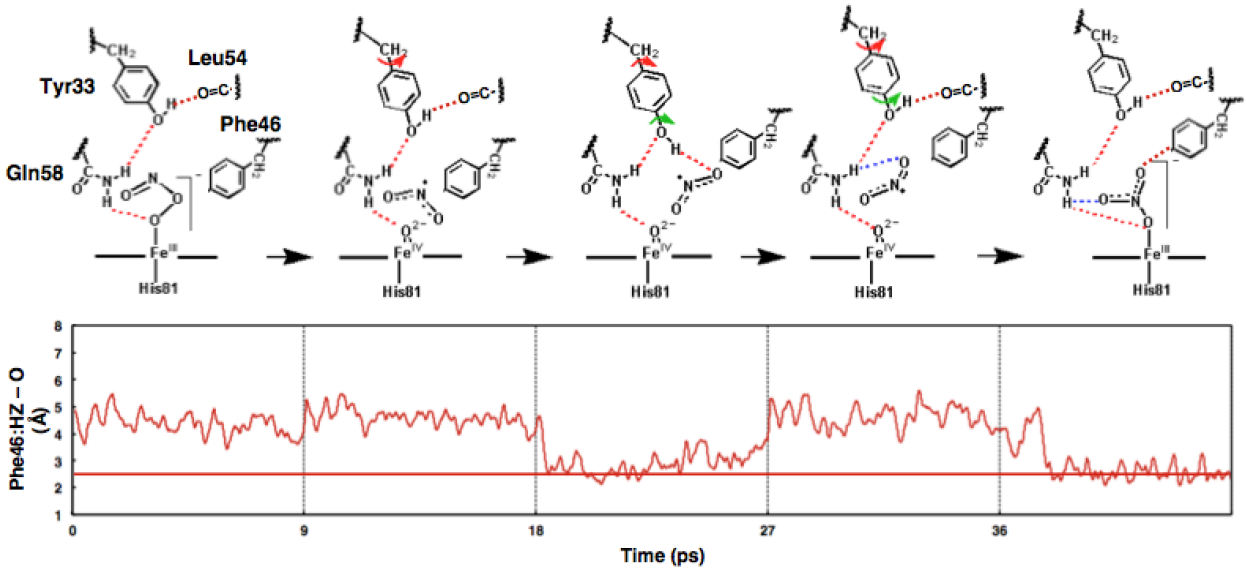

Figure 3.10 Phe46(CD1) stabilizes bound NO_3^- via C−H···O hydrogen bonding at H···O distances less than 2.40 Å comparable to those obtained from electronic structure calculations. See text for more details. C−H···O bond formed by Phe46(CD1) and bound NO_3^- is indicated with a red dashed line on the top schematic. Continuous horizontal line on the plot indicates stabilizing C−H···O hydrogen bond distances.

Phe32(B9), Val94(G8) prevent •NO_2 escape out of the active site and into the trHbN protein matrix. As mentioned previously, Phe32(B9), Val94(G8) and Gln58(E11) are the trHbN residues that dynamically reshape the entrance to the distal heme pocket giving access to the small apolar diatomic molecules (i.e. O_2, •NO) from the short-lived hydrophobic cavity corresponding to the experimentally identified xenon 2 binding site [23] which is located at the intersection of short, long and EH trHbN diffusion tunnels (see figure 1.2). The dynamics of Phe32(B9), Val94(G8) and Gln58(E11) residues do not only allow ligand/substrate diffusion into the distal heme cavity but, as observed from our simulations, they also block the exit of the •NO_2 reactive intermediate toward the interior of the trHbN protein. Furthermore, Tyr33(B10) and Phe46(CD1) residues prevent •NO_2 escape through trHbN BE tunnel and into the solvent.

Our simulations show that trHbN distal heme pocket residues Tyr33(B10), Gln58(E11), Phe46(CD1), Phe32(B9), and Val94(G8) isolate the highly reactive •NO_2 radical and prevent its escape toward the protein matrix where it could nitrate Tyr residues and lead to trHbN degradation. In trHbN there are two Tyr residues besides the distal Tyr33(B10).

Peroxynitrite heterolysis. Here we reported a sequential mechanism for the peroxynitrite isomerization reaction, which involves *homolysis* of the O-O peroxo bond to form oxo-ferryl species (compound II) and

•NO_2 radical. Analysis of the trajectories obtained from our constrained simulations did not reveal the formation of the nitrite anion (NO_2^-), the intermediate in the isomerization mechanism that involves the *heterolysis* of the peroxynitrite complex. Apart from the NO_2^- anion, the heterolytic O-O bond cleavage of the peroxynitrite complex would produce a compound I oxo-ferryl intermediate, and as hypothesized by Yeh et al [18] a Tyr33(B10) radical cation (Tyr33•$^+$) due to the presence of the nearby Tyr33(B10) in trHbN active site that could supply the redox equivalent needed for catalyzing the O-O bond cleavage. In this pathway, the oxo-ferryl iron would receive one electron from the nearby Tyr33(B10) (see section 1.3 for details on the heterolysis mechanism). However, the *large* distance (6.0 to 8.0 Å) between Tyr33(B10) and oxo-ferryl species as observed from our simulations (Figure 3.11) suggests that it may prohibit the electron transfer from Tyr33(B10) to the oxo-ferryl iron to occur (Marcus theory [51, 52]). Our results suggest that Tyr33(B10) may not be directly involved in the NOD isomerization reaction and agree with Crespo et al [32] earlier findings which indicated that Tyr33(B10) does not play a catalytic role in the NOD reaction. Using a Tyr33Phe mutant, Crespo et al [32] obtained very similar reaction energy profiles for wild-type trHbN and the Tyr33Phe variant and indicated that the trHbN catalyzed NOD isomerization reaction occurs mainly by means of the heme group [32]. In addition, it was mentioned above that the mechanism involving homolysis of the peroxynitrite O-O bond to produce •NO_2 is favored over the heterolytic mechanism producing nitrite NO_2^- given the relatively slow reaction of compound I with NO_2^- (16 $M^{-1} s^{-1}$) and the rapid reaction of compound II with •NO_2 (10^7 $M^{-1} s^{-1}$) [29, 34, 35].

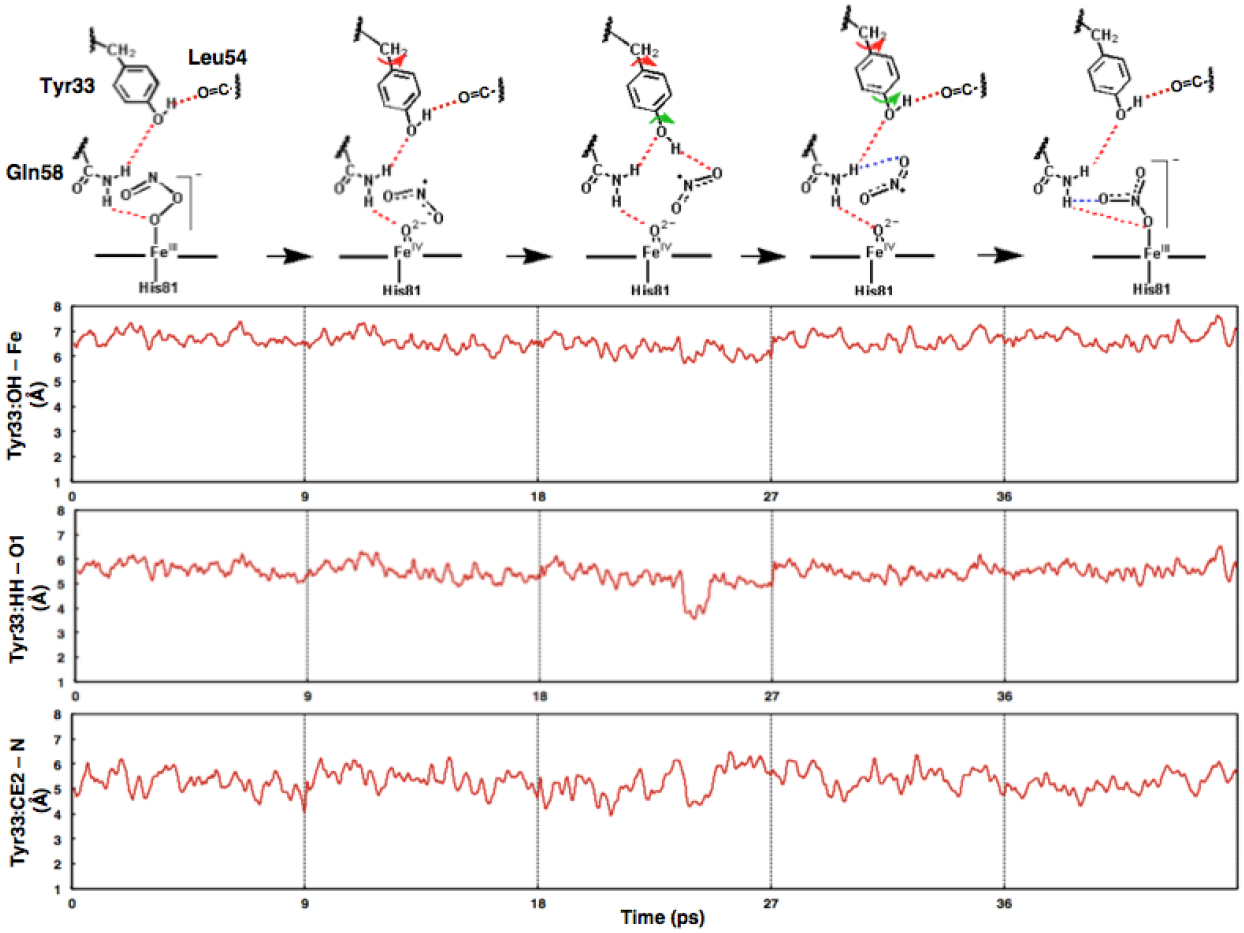

Figure 3.11 Time series for the distances between Tyr33(B10) hydroxyl group and oxo-ferryl species (*top two*) and between Tyr33(B10) CE2 atom at the third position of the phenyl group and the N-atom of $\bullet NO_2$ (*bottom*). The hydroxyl and phenyl groups of Tyr33(B10) are kept at a large distance relative to oxo-ferryl species and $\bullet NO_2$ by the H-bonding network between Tyr33(B10), Gln58(E11) and Leu54(E7) which prevents the oxidation and nitration of Tyr33(B10).

Tyr33(B10) nitration.

The presence of the distal Tyr33(B10) and highly reactive species, $Fe^{IV}=O^{2-}$ and $\bullet NO_2$, in the trHbN active site is problematic in principle. $Fe^{IV}=O^{2-}$ could readily oxidize Tyr33(B10) forming a tyrosyl radical (Tyr33•) and a ferric heme with hydroxide bound (Fe^{III}-OH^-), by electron transfer from Tyr33 to the ferryl iron to form a tyrosine radical cation (Tyr33$\bullet^+$) followed by proton abstraction from Tyr33 hydroxyl group by the ferric heme to form the tyrosyl radical (Tyr33•). The Tyr33• radical can then irreversibly interact with $\bullet NO_2$ to form 3-nitrotyrosine (see section 1.3 and figure 1.5 for details) that

could lead to permanent trHbN degradation and implicitly to the death of Mtb bacillus. As discussed previously, the electron transfer step in Tyr33(B10) oxidation may be prevented by the large distance between Tyr33(B10) and oxo-ferryl species (Figure 3.11; Tyr33(B10):OH–Fe distance). The distance between the H-atom of Tyr33(B10) hydroxyl group and O-atom of oxo-ferryl species (O1) is similarly large (Figure 3.11; Tyr33(B10):HH–O1 distance) and therefore prevent proton abstraction, and the oxidation of Tyr33(B10) to the tyrosyl radical (Tyr33•). Our simulations show that Tyr33(B10) is involved a continuous H-bonding network with Gln58(E11) and Leu54(E7) (see figure 3.6). The hydroxyl group H-atom of Tyr33(B10) continuously H-bonds with Leu54(E7) backbone and is oriented outward the active site, except when it transiently H-bonds the $\bullet NO_2$ intermediate and is oriented inward the active site. This correlates with changes in Tyr33(B10) orientation (see figure 3.7). In our simulations, Tyr33(B10) predominantly displays configurations where the Tyr33(B10) phenyl *ortho*-position (3-position; CE2 atom), where $\bullet NO_2$-mediated nitration damage can occur, is outward the active site and far from the $\bullet NO_2$ radical (Figure 3.11; Tyr33(B10):CE2–N distance). Our results indicate that *the H-bonding network between Tyr33(B10), Gln58(E11) and Leu54(E7) prevents the oxidation and nitration of Tyr33(B10) by keeping the hydroxyl and phenyl groups at "safe" distance and orientation relative to oxo-ferryl species and the $\bullet NO_2$ radical.*

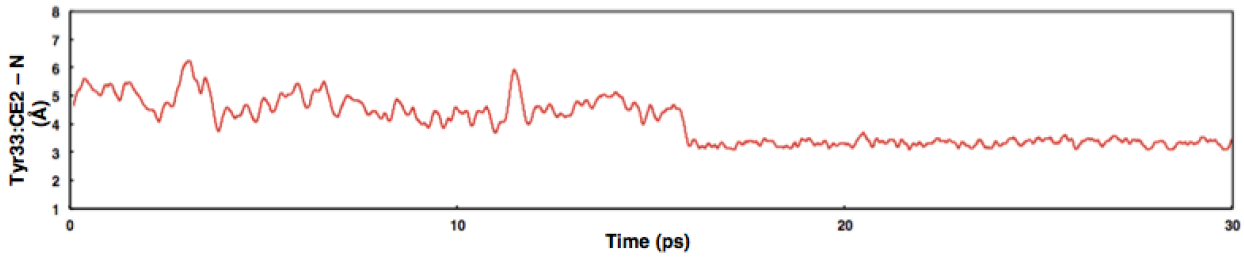

Figure 3.12 Evolution in time of Tyr33•–$\bullet NO_2$ distance obtained from a constrained QM/MM MD simulation with the distance between Tyr33(B10) hydroxyl hydrogen and the O-atom of oxo-ferryl species fixed at 0.95 Å. After 30 ps of simulation, $\bullet NO_2$ is closer to the presumed Tyr33• CE2 atom at third position, but 3-nitrotyrosine does not form. See text for details.

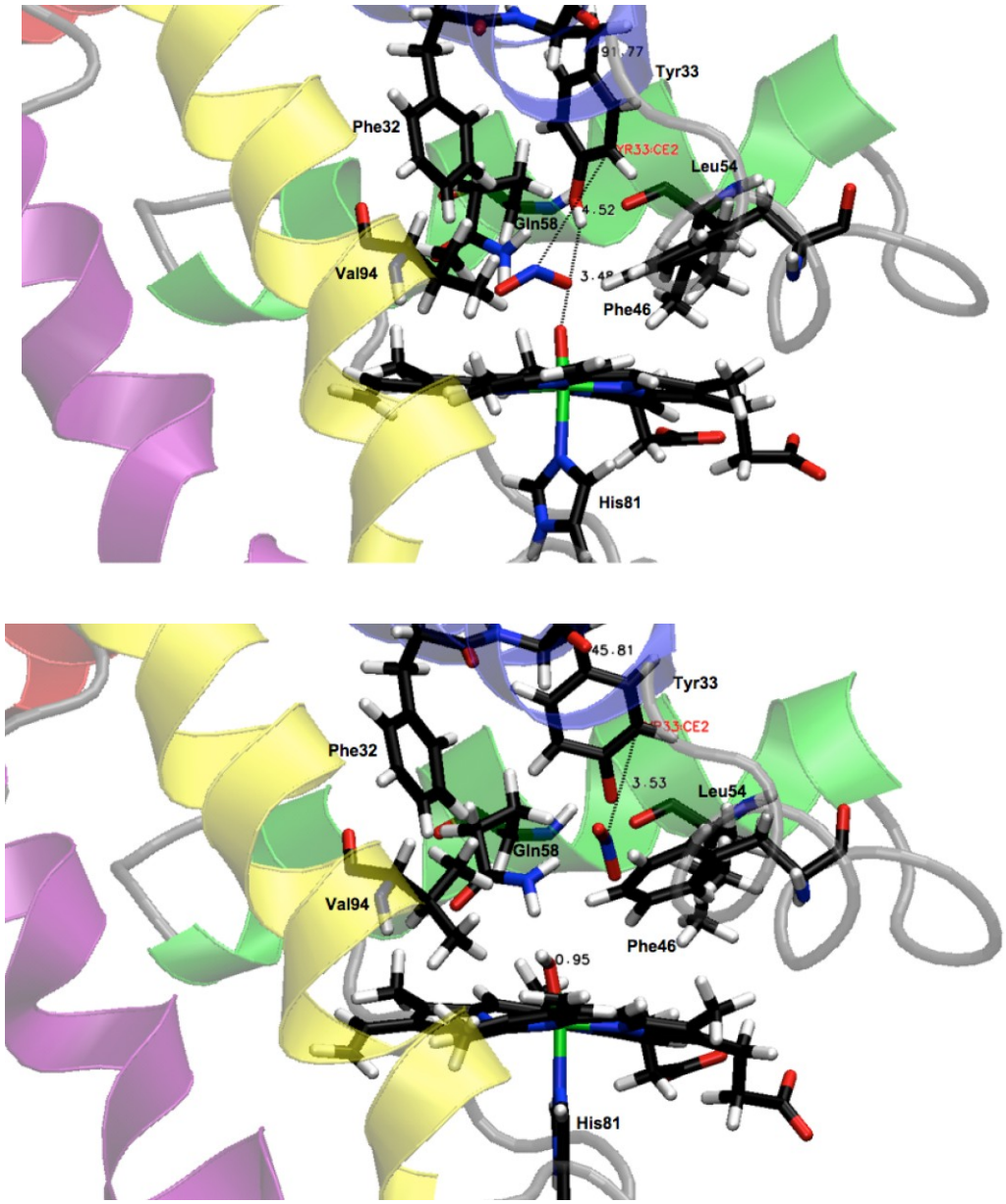

Figure 3.13 TrHbN active site at the start (*top*) of the constrained QM/MM MD simulation with the distance between Tyr33(B10) hydroxyl hydrogen and the O-atom of oxo-ferryl species fixed at 0.95 Å and after 30 picoseconds (*bottom*). •NO_2 radical gets closer to the presumed Tyr33• CE2 atom at third position but the Tyr33 phenyl ring rotates outward of the active site and further away from •NO_2, preventing its nitration. See text for details.

Nonetheless, to further investigate what prevents Tyr33(B10) nitration we performed constrained simulations QM/MM MD simulations with the Tyr33(B10):HH–O1 distance fixed at 0.95 Å, forcing the hydroxyl group proton abstraction by oxo-ferryl species, under the assumption that the electron transfer occurred, and thus Tyr33• formation. A snapshot from the sampling window where the $•NO_2$ radical is nearest the ortho-position of Tyr33 was selected as a starting structure. After 30 ps of simulation, the $•NO_2$ radical gets much closer to the presumed Tyr33• 3-position, relative to the starting structure (figure 3.12) yet the Tyr33 phenyl ring continues to rotate outward of the active site and further away from $•NO_2$, preventing its nitration (Figure 3.13).

Longer QM/MM MD simulations of wild-type TrHbN with Tyr33(B10):HH–O1 distance constrained may lead to the formation of 3-nitrotyrosine. Moreover, constrained simulations could be conducted with substitutions to small Ala for Gln58, Leu54, Phe46, Phe32 and Val94 residues that, as our results show, are crucial to obtain the fast reaction of $•NO_2$ with oxo-ferryl species, orient the nitrogen atom of $•NO_2$ away from Tyr33 phenyl ring and facilitate $•NO_2$ rebinding and stabilize the bound-product on the heme. These mutations would favor Tyr33• and 3-nitrotyrosine formations by DHP enlargement and loss of H-bonding networks observed and described above. Nonetheless, our results suggest that Tyr33(B10) nitration does not occur.

3.3 Discussion

Our results show a sequential mechanism with very short-lived intermediates for the heme-catalyzed isomerization reaction in trHbN of Mtb. This is in agreement with Crespo et al [32] but contrary to Mishra et al [33] earlier theoretical studies. As far as possible intermediates of the NOD isomerization reaction are concerned, there have been no experimental kinetics studies for trHbN. However, our results suggest that they may be too short-lived to be detected experimentally. Our results provide strong evidence that the highly-conserved residues Tyr33(B10), Gln58(E11), Leu54(E7), Phe46(CD1) and Phe32(B9) in trHbN's distal heme pocket facilitate and cage the highly reactive intermediates of the isomerization reaction, thus substantiating an earlier hypothesis of Crespo et al [32]. Analysis of trajectories obtained from our constrained QM/MM MD simulations show that, the hydrogen bonding network formed between Tyr33(B10), Gln58(E11) and ligands includes Leu54(E7), a fact that, to our knowledge, has not been reported before. Mishra et al [33] found that, during the $•NO_2$ rebinding step, $•NO_2$ continuously participates in H-bonding with both Tyr33(B10) and Gln58(E11), while our results show that Tyr33(B10) stabilizes the radical $•NO_2$ transiently, being prevalently H-bonded to Leu54(E7). Moreover, our results show that concerted motions of Tyr33(B10), Gln58(E11) and Phe46(CD1) assist

•NO_2 rebinding and stabilize the bound nitrate. The conformational changes of Tyr33(B10) and the stabilization of bound product by Phe46(CD1) that our results show, have not been reported to date. In addition, the oxidation and nitration of Tyr33(B10) (of trHbN) have not been investigated before. Our results suggest that the H-bonding network between Tyr33(B10), Gln58(E11) and Leu54(E7) prevents Tyr33(B10) oxidation and nitration, and trHbN itself degradation, by keeping the hydroxyl and phenyl groups at "safe" distance and orientation relative to oxo-ferryl species and the •NO_2 radical.

Our new insights on the mechanism and the role of trHbN environment in the heme-catalyzed isomerization reaction and the discrepancies with earlier theoretical studies originate primarily from the methodologies used. We employed free energy calculations using constrained QM/MM MD simulations, thus incorporating the effects of thermal fluctuations, the rearrangement of trHbN residues at the active site and extensive sampling in two dimensions. On the other hand, Crespo et al [32] employed QM/MM restrained geometry optimizations along one-dimensional predefined reaction coordinates for the elementary steps of the isomerization reaction. The method lacks nuclear dynamics and conformational sampling. An additional term is introduced in the potential energy of the system to penalize any deviation of a reaction coordinate from a reference value. Mishra et al [33] employed the adiabatic reactive molecular dynamics (ARMD) method that allows for sufficiently long molecular dynamics simulations, nonetheless ARMD is a simple potential energy surface crossing approach to study reactive processes, within the classical MD framework. The method involves the parameterization of potential energy surfaces of the reactants and the products with individual force fields.

Chapter 4
NOD Reaction: Product release

Dissociation of the nitrate anion, the product of the NOD reaction, involves the breaking of the bond between the anion and the heme group, and a change in the heme coordination from hexa- to penta-coordinated, presuming no other ligand comes in. In addition to the breaking of the Fe^{III}-O bond in the heme-bound nitrato complex, the release of the nitrate anion to the aqueous environment involves the diffusion of the anion through the protein matrix. Marti et al [25] simulated the release of the nitrate anion by Mtb trHbN. Their molecular dynamics simulations suggest that the formation of the ferric-nitrato species causes a structural distortion of the distal heme pocket cavity walls that forms pores for water entry. The structural destabilization affects, among other residues, Phe46(CD1), the residue that shields the heme from the solvent, the side-chain of which rearranges to open a pathway for water entry [25]. Moreover, their QM(B3LYP/LACV3P*)/MM energy minimizations, using a reduced gas-phase-like model which includes in the QM subsystem only the heme group, the nitrate anion and the axial histidine, and a model in which water molecules H-bonded to the nitrate anion are added to the QM part, suggest that water hydration weakens the bond between the heme iron atom and nitrate anion [25]. Once the Fe^{III}-O bond is broken, the nitrate anion exits in ~5 ns via a unique pathway distinct from O_2 and NO tunnels [25, 22, 23]. A role for ThrE2 in assisting nitrate egress has been proposed [25]. Furthermore, Marti et al's QM/MM energy minimizations with Tyr33(B10) and Gln58(E11) residues included in the QM subsystem [25] pointed out that the Tyr33(B10)/Gln58(E11) pair is crucial for breaking the Fe^{III}-O bond of the heme-bound nitrato complex. Similarly, Mishra et al's [33] ARMD simulations with trHbN and its mutants Tyr(B10)Ala and Gln(E11)Ala indicated that Tyr33(B10) and Gln58(E11) strongly influence nitrate dissociation. Here we investigate nitrate dissociation both in gas phase and trHbN environment. We specifically aim to understand the role of Tyr33(B10)/Gln58(E11) pair and also of Phe46(CD1) and Phe32(B9) residues in promoting product dissociation and release.

4.1 Gas-phase model for nitrate release

QM(DFT) geometry optimizations were carried out to investigate the product dissociation in gas phase. The Fe-N distance was used as the reaction coordinate to obtain the energy profile for nitrate dissociation (Figure 4.1). Geometry optimizations were performed with the Fe-N reaction coordinate scanned from 2.75 to 6.00 Å, in 0.25 Å increments and using a reduced model, which included the porphyrin-imidazole complex and the nitrate anion. The energy profile shows that the global minimum is for the bound-nitrate

obtained from the QM(DFT) calculation at a Fe-N distance of 3.00 Å, which corresponds to a Fe-O1 distance of 1.92 Å. This distance is in good agreement with the value of 1.97 Å obtained by Marti et al [25] from gas phase QM(DFT) calculations using a similar model chemistry and the same reduced model. Nitrate is fully dissociated at Fe-N distances larger than 4.75 Å corresponding to Fe-O1 distances greater than 3.76 Å. The energetic difference between bound-nitrate and released product is 35 kcal/mol (at 6.00 Å Fe-N distance). The optimized geometries obtained from gas phase calculations (Figure 4.1) indicate that in bound form or at Fe-N distances in the 3.00 to 4.75 Å range the nitrate anion is coplanar with the imidazole ring and perpendicular to the porphyrin ring, while at Fe-N distances larger than 4.75 Å the product gradually tilts to the side of the porphyrin ring.

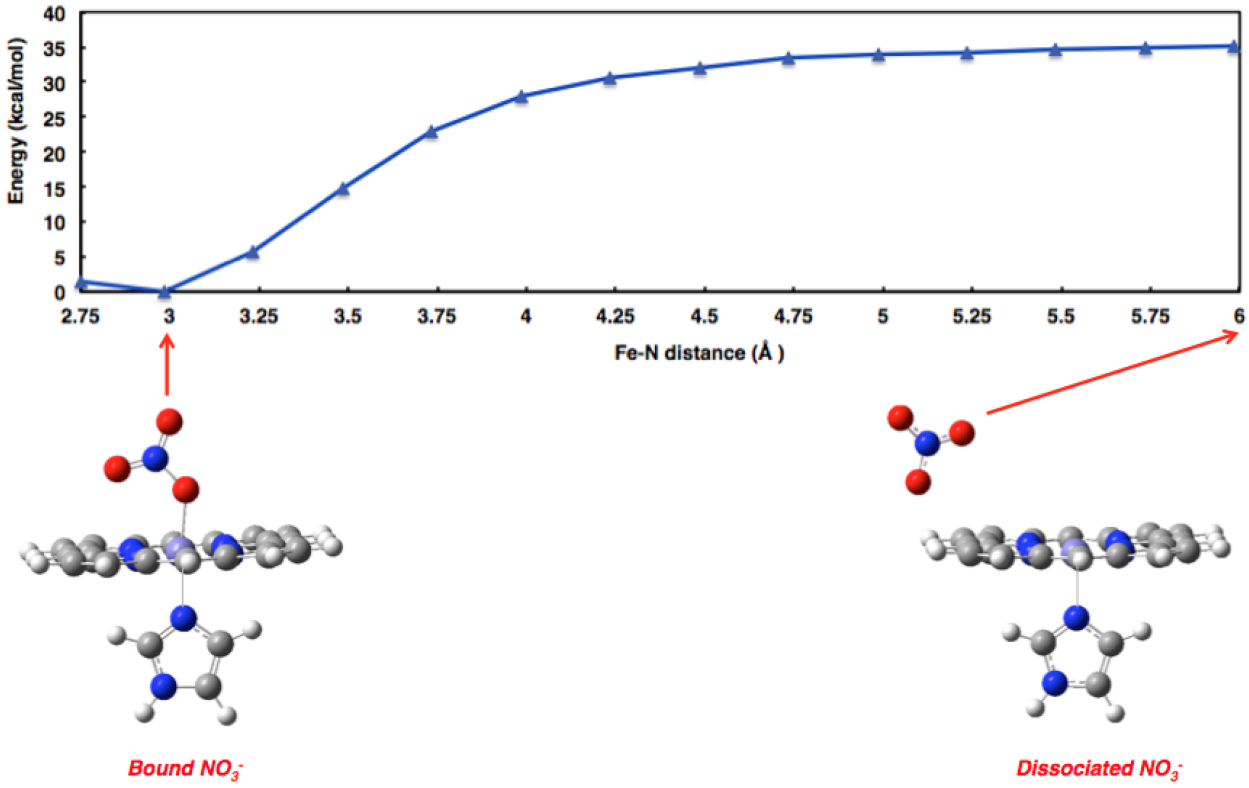

Figure 4.1 One-dimensional potential energy surface (1D PES) of NO_3^- dissociation in gas phase. Optimized structures of bound and dissociated NO_3^- are indicated with red arrow at distance of 3.00 Å and 6.00 Å, respectively.

4.2 Nitrate release in trHbN environment

Constrained QM/MM MD simulations were conducted to investigate the dissociation and release of the nitrate anion in trHbN environment and to understand the role of Tyr33(B10)/Gln58(E11) pair and also Phe46(CD1) and Phe32(B9) active site residues in promoting the dissociation and release. A one-dimensional PMF for product release was constructed by straightforward numerical integration of the average mean forces obtained from the constrained simulations using the trapezoidal rule. Similarly to the gas-phase calculations, the Fe-N distance was chosen as a reaction coordinate. The Fe-N reaction coordinate was constrained, in 14 sampling windows, at distances in the 2.75 to 6.00 Å range and scanned in increments of 0.25 Å.

Energetics.

Figure 4.2 shows the 1D PMF constructed for the product release. Similarly to the gas-phase calculations, the minimum free energy on the 1D PMF corresponds to the bound-nitrate and was obtained from the simulation window having the Fe-N reaction coordinate constrained at 3.00 Å. The maximum free energy on the 1D PMF profile, in simulation window with Fe-N distance constrained at 4.00 Å, indicates a transition state-like energetic barrier of 11.5 kcal/mol. Nitrate dissociation can thus be estimated to occur on microsecond timescale. Such a time constant suggests that nitrate dissociation may be the rate-liming step in the overall NOD reaction. Nonetheless, the estimated rate constant must be interpreted as an upper limit given that nitrate dissociation and release may be favored by the inclusion of water molecules in the distal heme pocket. Waters could hydrate the nitrate anion or coordinate the ferric iron thus speeding up the nitrate dissociation step and justifying the rapid overall NOD reaction. Worth mentioning is that throughout our simulations, bulk waters or NO molecules (9 out of 10 total) included in the MM part of the simulation system never entered the distal heme pocket. This was to be expected since QM/MM simulations are very short. At Fe-N distances larger than 4.00 Å, the free energy goes downhill to the product state.

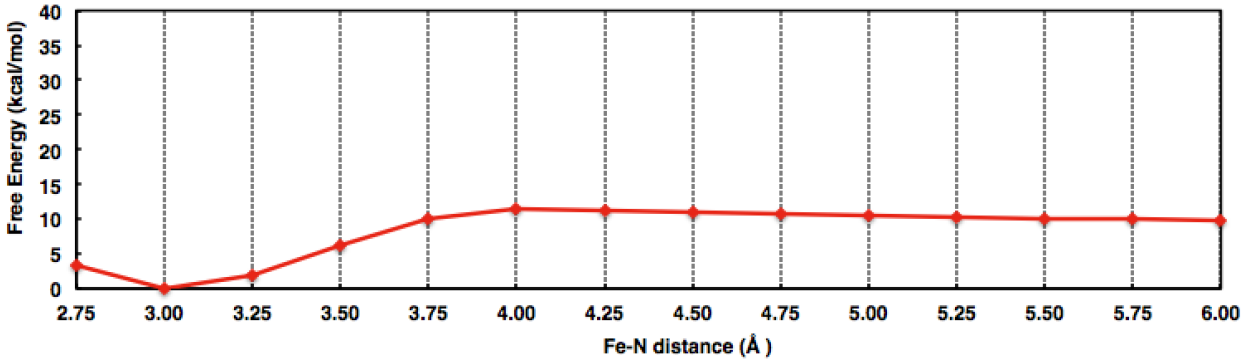

Figure 4.2 One-dimensional potential of mean force (1D PMF) of NO_3^- dissociation in trHbN environment. Vertical dashed lines delimit the sampling windows were constrained QM/MM MD simulation were performed at fixed Fe-N reaction coordinate. See text for details.

TrHbN dynamics.

Marti et al's [25] QM/MM energy minimizations with Tyr33(B10) and Gln58(E11) residues included in the QM subsystem pointed out that the Tyr33(B10)/Gln58(E11) pair is crucial for breaking the Fe^{III}-O bond of the heme-bound nitrato complex. Similarly, Mishra et al ARMD simulations with wild-type trHbN and its mutants Tyr(B10)Ala and Gln(E11)Ala [33] indicated that Tyr33(B10) and Gln58(E11) strongly influence nitrate dissociation. Our results substantiate the fact that the electrostatic interactions between the nitrate anion and Tyr33(B10)/Gln58(E11) pair promote NO_3^- dissociation and are the main stabilizing residues for the product. Moreover, we show that the interactions between the aromatic residues Phe46(CD1), Phe32(B9) and Tyr(B10) and the nitrate anion are not energetically negligible and thus contribute to the stabilization of the dissociated product and its release by forming interactions such as those presented in Figure 3.9.

Tyr33(B10)/Gln58(E11) pair promote NO_3^- dissociation. NO_3^- product is participating in the Tyr33(B10), Gln58(E11), Leu54(E7) dynamic hydrogen-bonding network.

Analysis of trajectories obtained from the simulations of nitrate release show that the *hydrogen-bonding network between Tyr33(B10), Gln58(E11) and Leu54(E7)* formed in the previous steps of the NOD reaction is maintained during the NO_3^- dissociation step. The H-bond between Tyr33(B10) and Gln58(E11) is very stable with an average Tyr33(B10):OH–Gln58(E11):HE22 distance of 2.20 Å in the simulation windows where the Fe-N reaction coordinate is constrained at distances in the 2.75 Å and 4.00 Å range (the latter the barrier for NO_3^- dissociation toward free product) (Figure 4.3). At larger Fe-N distances, the Tyr33(B10):OH–Gln58(E11):HE22 H-bond breaks transiently due to the fact that

Gln58(E11):HE22 hydrogen atom H-bonds the oxygen atoms of the NO_3^- ligand (Figure 4.5). The H-bond formed between Tyr33(B10) hydroxyl H atom and the carbonyl O atom of Leu54(E7) backbone is also very stable throughout the dissociation process as shown in figure 4.3 (1.9 Å Tyr33(B10):HH–Leu54(E7):O distance average). Noteworthy, the Tyr33(B10):HH–Leu54(E7):O H-bond is lost for several picoseconds in 5 simulations windows when Tyr33(B10) conformation changes significantly (Figure 4.3) and stabilizes the NO_3^- anion via H-bonding (Figure 4.4). The 5 simulation windows are and illustrated in figure 4.3 and enlisted below:

(W1) Fe-N reaction coordinate distance of 3.00 Å corresponding to nitrate bound to ferric iron,

(W2, W3, and W4) Fe-N distances of 3.50, 3.75, and 4.25 Å when the Fe^{III}-O bond of the nitrato-complex weakens, breaks, and NO_3^- dissociates, and

(W5) Fe-N distance of 5.00 Å when NO_3^- is fully dissociated.

Tyr33(B10) changes conformation during product dissociation.

The loss of Tyr33(B10):HH–Leu54(E7):O H-bond correlates with changes in Tyr33(B10) conformation, specifically with Tyr33(B10) hydroxyl group rotation as evidenced by the time series for the HH-OH-CZ-CE2 dihedral angle (figure 4.3). Tyr33(B10) dynamics are similar to those described earlier for the NOD isomerization reaction. During the NO_3^- dissociation process, though, Tyr33(B10) does not rotate significantly around the CB-CG bond, in other words there are no atypical changes in the $\chi 2$ dihedral angle and no flip of the phenyl group. As mentioned above, Tyr33(B10) conformation changes significantly in 5 simulation windows:

(W1) At Fe-N distance of 3.0 Å, Tyr33(B10) hydroxyl group rotates by ~210° inward the heme pocket cavity stabilizing the bound-nitrate;

(W2, W3, and W4) At Fe-N distances of 3.50, 3.75 and 4.25 Å, Tyr33(B10) hydroxyl group rotates again (~220°) to assist (in conjunction with Gln58(E11) – see below) the breaking of Fe^{III}-O bond of the nitrato-complex, and NO_3^- dissociation; and

(W5) At Fe-N distance of 5.00 Å when NO_3^- is fully dissociated, Tyr33(B10) turns inward once more and the HH-OH-CZ-CE2 dihedral angle changes by as much as 240° to help pull the NO_3^- product out of the active site.

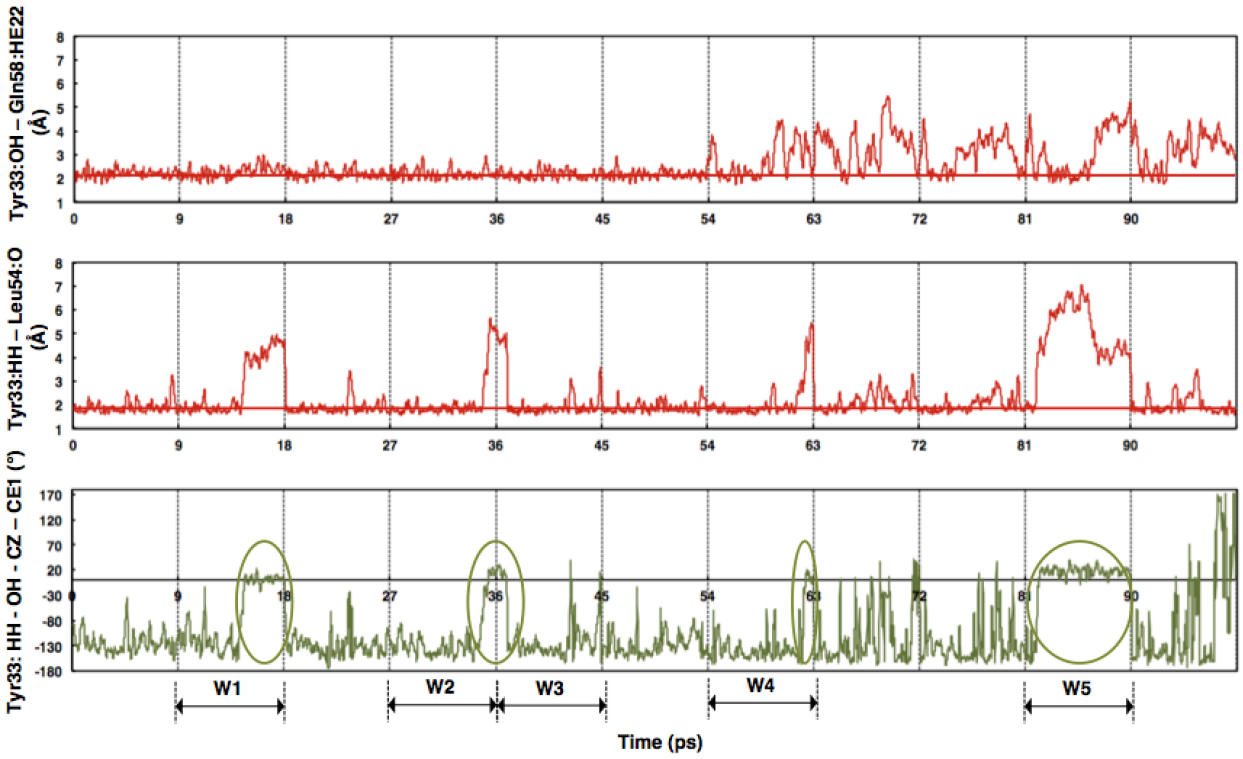

Figure 4.3 Tyr33(B10)/Gln58(E11)/Leu54(E7) dynamic hydrogen-bonding network and Tyr33(B10) conformational changes that promote NO_3^- dissociation. Dashed lines delimit individual 9 picoseconds constrained simulations for product release. W1 to W5 identify simulation windows where Tyr33(B10) changes conformations and oriented inward the active site. (W1) Fe-N reaction coordinate distance of 3.00 Å corresponding to nitrate bound to ferric iron, (W2, W3, and W4) Fe-N distances of 3.50, 3.75, and 4.25 Å when the Fe^{III}-O bond of the bound nitrate weakens, breaks, and NO_3^- dissociates, and (W5) Fe-N distance of 5.00 Å when NO_3^- is fully dissociated. The details of the dynamics are explained in the text.

Tyr33(B10) stabilizes the NO_3^- anion via H-bonding.

The Tyr33(B10) rotations orient the hydroxyl group inward the active site and cause the formation of transient stabilizing H-bonds between Tyr33(B10) hydroxyl hydrogen and the oxygen atoms of the NO_3^- product (figure 4.4) in the 5 simulation windows discussed above. Interestingly, in the simulation window in which the Fe-N distance was constrained at 5.0 Å (W5), for almost 3 picoseconds, NO_3^- abstracts the proton from the Tyr33(B10) hydroxyl hydrogen atom to form nitric acid. After this event, the tyrosinate takes back its proton and continues to H-bond the NO_3^- product (as it did at the beginning of the simulation), assisting its release.

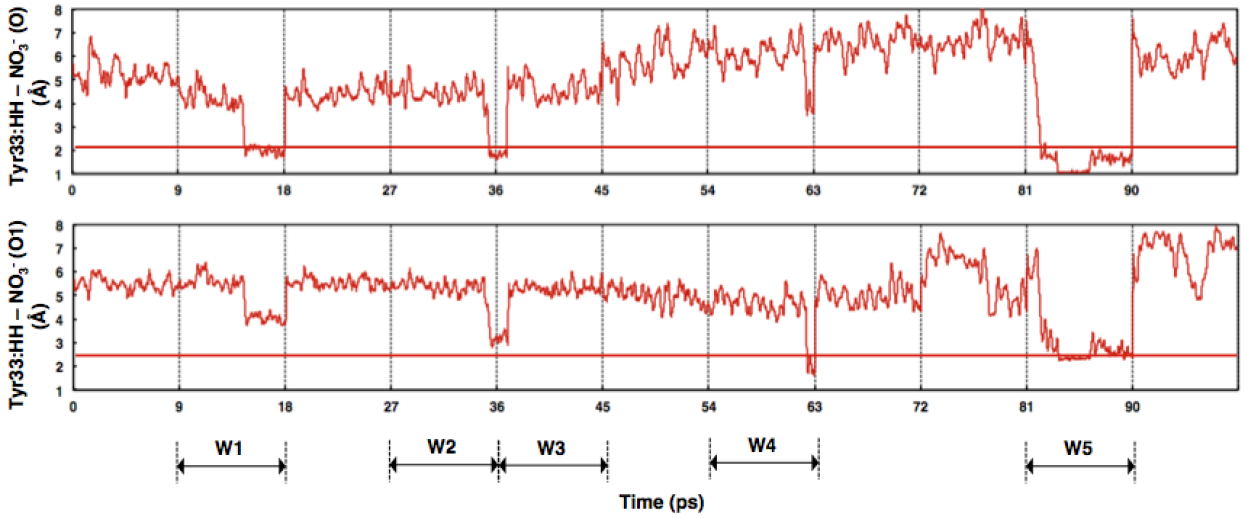

Figure 4.4 Tyr33(B10) stabilizes the NO_3^- anion via H-bonding. See text for details.

Gln58(E11) is a H-bond donor to the NO_3^- oxygen atoms and the main stabilizing residue for the NO_3^- anion in both bound and dissociated forms.

It was mentioned previously that Gln58(E11) and Tyr33(B10) form a very stable H-bond in all sampling windows having the Fe-N reaction coordinate constrained at distances in the 2.75 and 4.00 Å range. At larger Fe-N distances, though, the Tyr33(B10):OH–Gln58(E11):HE22 H-bond breaks transiently due to the fact that Gln58(E11):HE22 hydrogen atom of its amide group H-bonds the oxygen atoms of the NO_3^-, stabilizing it as it starts diffusing out of the active site (Figure 4.5). In addition, for Fe-N reaction coordinate in the 3.00 Å and 3.75 Å range, Gln58(E11):HE22 hydrogen atom also forms a very stable H-bond with the O atoms of nitrate both in bound form and as it dissociates off the ferric iron (Figure 4.5). Furthermore, the Gln58(E11):HE21 hydrogen atom of the amide group forms H-bonds with the O atoms of the nitrate anion throughout the entire release process. As shown in figure 4.5 for Fe-N reaction coordinate in the 3.00 Å and 3.75 Å range, Gln58(E11):HE21 hydrogen atom forms a very stable H-bond with both O and O1 atom of nitrate ligand, pulling it off the ferric iron. At larger Fe-N distances, Gln58(E11):HE21 hydrogen atom H-bonds the O2 atom of the NO_3^- anion mostly, but also O and O1 atoms, as the anion tumbles between two orientations: a parallel and a perpendicular T-like orientation relative to the plane of the heme macrocycle, respectively. These findings suggest that Gln58(E11) contributes substantially to the breaking of the Fe^{III}-O bond of bound nitrate by pulling it off the ferric iron and to the stabilization of the dissociated nitrate on its way out of the heme pocket cavity.

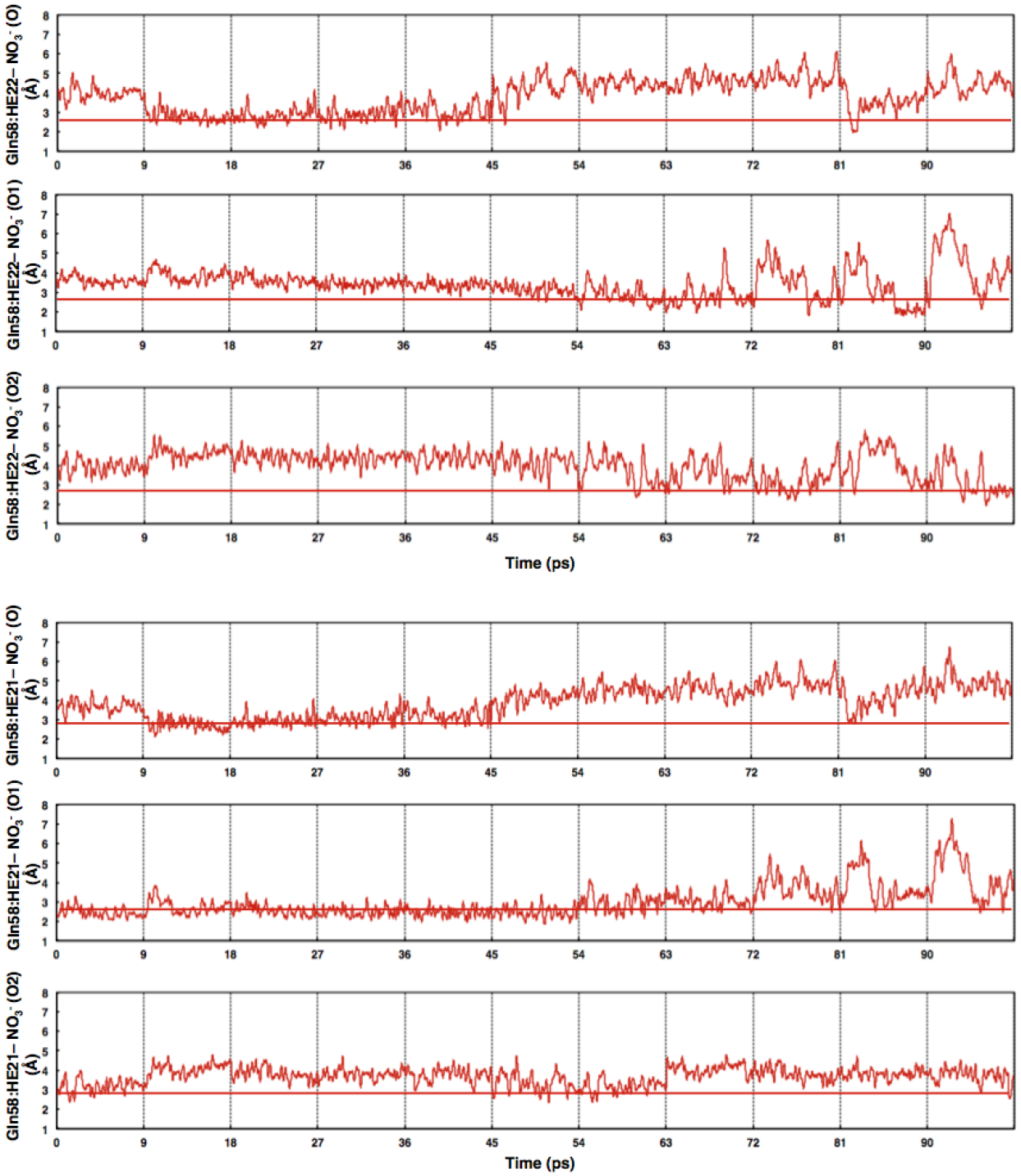

Figure 4.5 Gln58(E11) is the main stabilizing residue for the NO_3^- anion in both bound and dissociated forms. See text for details. Continuous horizontal red lines indicate stabilizing hydrogen bonding distances.

Phe46(CD1), Phe32(B9) and Tyr33(B10) aromatic side-chains favorably interact with NO_3^- and contribute to its release.

We showed previously that Phe46(CD1) stabilizes bound NO_3^- by C−H···O hydrogen bonding at H···O distances less than 2.40 Å, which correspond to C−N distances less than 4.00 Å. At these distances, the interactions between the aromatic side-chains of Phe46(CD1), Phe32(B9) and Tyr33(B10) residues and nitrate anion are not negligible and contribute to the stabilization of the anion as it dissociates and gets further away from the active site (Figure 4.6).

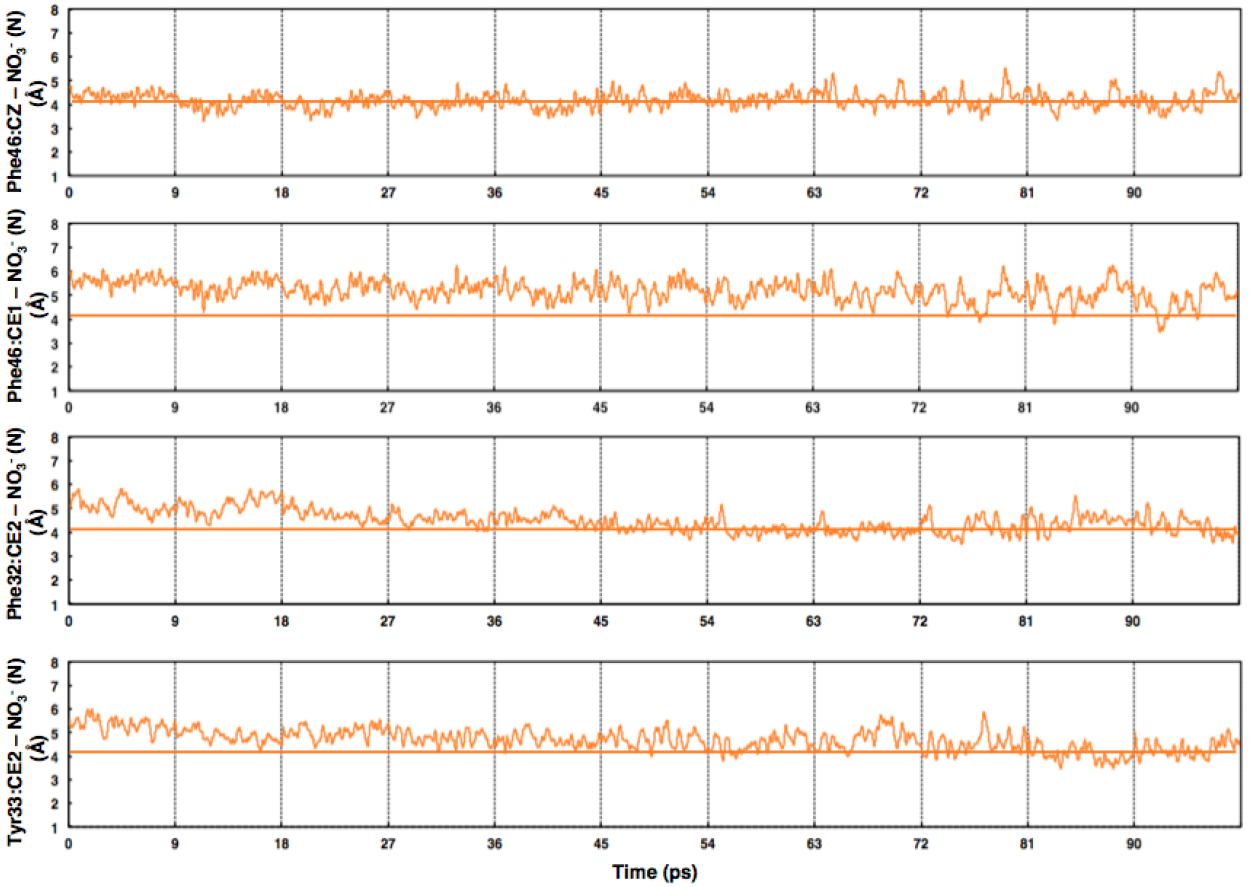

Figure 4.6 Phe46(CD1), Phe32(B9) and Tyr33(B10) aromatic side-chains favorably interact with NO_3^- and contribute to its release, via C−H···O hydrogen bonding. Continuous horizontal orange lines indicate stabilizing interactions.

4.3 Discussion

Our results substantiate earlier theoretical results [25, 33] that the electrostatic interactions between the nitrate anion and Tyr33(B10)/Gln58(E11) pair promote NO_3^- dissociation and are the main stabilizing residues for the product. Moreover, we show that the interactions between the aromatic residues Phe46(CD1), Phe32(B9) and Tyr(B10) and the nitrate anion contribute to the stabilization of the dissociated product and its release. Water entry into the distal heme pocket cavity, which could promote NO_3^- dissociation as suggested by Marti el al [25], was not observed in our short QM/MM MD simulations. Based on our current results, we cannot indicate whether the long tunnel or the BE tunnel is used for product release.

Chapter 5
Conclusion

In this study, the nitric oxide dioxygenase (NOD) reaction of the truncated hemoglobin N (trHbN) from *Mycobacterium tuberculosis* (Mtb) was investigated using state-of-the-art computational methods. QM(DFT) geometry optimizations were performed to model the reaction in gas-phase. Constrained QM/MM MD simulations were carried out to study the NOD reaction in trHbN environment. Here we report our findings on the mechanism, reaction intermediates and protein dynamics during the NOD reaction. The results suggest a sequential mechanism for the NOD isomerization reaction with very short-lived intermediates, which may not be detected experimentally. Distal Gln58, Tyr33, Leu54, Phe46, Phe32 and Val94 residues facilitate and cage the highly reactive $Fe^{IV}=O^{2-}$ and $\bullet NO_2$ intermediates that result from $OONO^-$ homolysis. Tyr33 is involved in a dynamic H-bonding network with Gln58 and Leu54. Tyr33 changes conformations during the reaction and transiently stabilizes the $\bullet NO_2$ radical. Gln58 stabilizes the O-atom of oxo-ferryl species and assists $\bullet NO_2$ rebinding via H-bonding. Phe46 stabilizes the bound product. Our results suggest that Tyr33 is not directly involved in the isomerization reaction. The H-bonding network between Tyr33, Gln58 and Leu54 prevents the oxidation and nitration of Tyr33 by keeping the phenyl ring at safe distance and orientation with respect to oxo-ferryl species. Similar dynamics of the distal heme pocket residues have been observed for NO_3^- dissociation and release. Tyr33, Gln58, Phe46 and Phe32 stabilize NO_3^- via H-bonding, and promote the breaking the Fe^{III}-O bond of the bound NO_3^-, its dissociation and release. By controlling the isomerization reaction, trHbN prevents its own degradation and plays a critical role in Mtb survival and in the persistence of tuberculosis. TrHbN has no human homolog and as such is a potential allosteric target in the treatment of tuberculosis. Our methods could be employed in theoretical investigations aimed at providing mechanistic insights into chemical reactions catalyzed by heme proteins. Our results suggest that the mechanism of the NOD reaction catalyzed by trHbN of Mtb is similar in bacterial flavoHbs having two polar groups and three aromatic side-chains in the distal heme pocket, but different in mammalian globins functioning as NODs which have one polar group and three aliphatic residues in the distal pocket.

Bibliography

1. Gutierrez, M. C., Brisse, S., Brosch, R., Fabre, M., Omaïs, B., Marmiesse, M., Supply, P., and Vincent, V. (2005) PLoS Pathog 1 (1): e5

2. Brosch, R., Gordon, S. V., Marmiesse, M., Brodin, P., Buchrieser, C., Eiglmeier, K., Garnier, T., Gutierrez, C., Hewinson, G., Kremer, K., Parsons, L. M., Pym, A. S., Samper, S., van Soolingen, D., and Cole, S. T. (2002) PNAS 99 (6), 3684–3689

3. Smith, I., (2003) Clin. Microbiol. Rev. 16 (3), 463-496

4. Daniel, T.M. (2006) Respiratory Medicine 100 (11), 1862-1870

5. http://www.who.int/tb/publications/global_report/en/; last accessed: August 6, 2014

6. http://www.cdc.gov/nchhstp/newsroom/docs/TB-Drug-Resistance-FactSheet.pdf; last accessed: August 6, 2014

7. http://www.tballiance.org/why/mdr-xdr.php; last accessed: August 6, 2014

8. Pieters, J. (2008) Cell Host & Microbe 3, Elsevier Inc.

9. Mackaness, G. B. (1962) J Exp Med. 116, 381–406

10. Druszczynska, M., Kowalewicz-Kulbat, M., FOL, M., Włodarczyk, M., and Rudnicka, W. (2012) Polish Journal of Microbiology 61 (1), 3-10

11. Chan, J., Xing, Y., Magliozzo, R. S., and Bloom B. R. (1992) J. Exp. Med. 175, 1111-1122

12. Gardner, P. R. (2012) Scientifica Vol 2012, Article ID 683729, 34 pages Hindawi Publishing Corporation http://dx.doi.org/10.6064/2012/683729

13. Radi, R. (2004) Proc. Natl. Acad. Sci. 101 (12), 4003-4008

14. Ouellet, H., Ouellet, Y., Richard, C., Labarre, M., Wittenberg, B., Wittenberg, J., and Guertin, M. (2002) Proc. Natl. Acad. Sci. USA 99, 5902-5907

15. Couture, M., Yeh, S. R., Wittenberg, B., Wittenberg, J., Ouellet, Y., Rousseau, L., and Guertin, M. (1999) Proc. Natl. Acad. Sci. USA 96, 11223-11228

16. Milani, M., Pesce, A., Nardini, M., Ouellet, H., Ouellet, Y., Dewilde, S., Bocedi, A., Guertin, M., Moens, L., Friedman, J. M., Wittenberg, J. B., and Bolognesi, M. (2005) J. Inorg. Biochem. 99, 97-109

17. Gardner, P. R., (2005) J. Inorg. Biochem. 99 247- 266

18. Yeh, S. R., Couture, M., Ouellet, Y., Guertin, M., and Rousseau, D. L. (2000) J. Biol. Chem. 275, 1679-1684

19. Milani, M., Pesce, A., Ouellet, Y., Ascenzi, P., Guertin, M., and Bolognesi, M. (2001) EMBO J. 20, 3902-3909

20. Ascenzi, P., Bolognesi, M., Milani, M., Guertin, M., and Visca, P. (2007) Gene 398, 42-51

21. Lama, A., Pawaria, S., Bidon-Chanal, A., Anand, A., Gelpi, J. L., Arya, S., Marti, M., Estrin, D. A., Luque, F. J., and Dikshit K. L. (2009) J. Biol. Chem. 284 (21), 14457-14468

22. Bidon-Chanal, A., Marti, M. A., Crespo, A., Milani, M., Orozco, M., Bolognesi, M., Luque, F. J., and Estrin, D. A. (2006) Proteins: Struct., Funct., Bioinf. 64, 457-464

23. Daigle, R., Rousseau, J. A., Guertin, M., and Lagüe, P. (2009) Biophys. J. 97 (11), 2967-2977

24. Daigle, R., Rousseau, J. A., Guertin, M., and Lagüe, P. (2009) Proteins 75, 735-747

25. Marti, M. A., Bidon-Chanal, A., Crespo, A., Yeh, S. R, Guallar, V., Luque, F. J., and Estrin, D. A., (2008) J. Am. Chem. Soc. 130, 1688-1693

26. Möller, M. N., Lancaster Jr., J. R., and Denicola, A. In Free Radical Effects on Membranes; Matalon, S., Ed.; Current Topics in Membranes; Academic Press, 2008; Vol. 61; pp 23-42

27. Snider, C., Jayasinghe, S., Hristova, K., and White, S. H. (2009) Protein Sci. 18, 2624-2628

28. Johnson, J., and Cornell, R. (1999) Mol. Membr. Biol. 16, 217-235

29. Herold, S., Matsui, T., and Watanabe, Y. (2001) J. Am. Chem. Soc. 123 4085-4086

30. Gardner, A. M., Martin, L. A., Gardner P. R., Dou, Y., and Olson J. S. (2000) J. Biol. Chem. 275 12581-12589

31. Blomberg, L. M., Blomberg, M. R. A., and Siegbahn P. E. M. (2004) J. Biol. Inorg. Chem. 9, 923-935

32. Crespo, A., Marti, M. A., Kalko, S. G., Morreale, A., Orozco, M., Gelpi, J. L., Luque, F. J., and Estrin, D. A. (2005) J. Am. Chem. Soc. 127, 4433-4444

33. Mishra, S., and Meuwly, M. (2010) J. Am. Chem. Soc. 132, 2968-2982

34. Herold, S. (1999) FEBS Letters 443 81-84

35. Herold, S., and Rehmann, F-J. K. (2003) Free Radical Biology & Medicine, Vol. 34, No. 5, pp. 531-545

36. Yukl, E. T., de Vries, S., and Moënne-Loccoz, P. (2009) J Am Chem Soc. 131, 7234–7235

37. Bourassa, J. L., Ives, E. P., Marqueling, A. L., Shimanovich, R., and Groves, J. T. (2001) J. Am. Chem. Soc. 123, 5142-5143

38. Su, J., and Groves, J. T. (2010) Inorg. Chem. 49, 6317-6329

39. Gardner, P. R., Gardner, A. M., Brashear, W. T., Suzuki, T., Hvitved, A. N., Setchell, K. D. R., and Olson, J. S. (2006) J. Inorg. Biochem. 100, 542-550

40. Bryantsev, V.S., and Hay, B. P. (2005) J. Am. Chem. Soc. 127 (23), 8282-8283

41. Frisch, M. J., Trucks, G. W., Schlegel, H. B., Scuseria, G. E., Robb, M. A., Cheeseman, J. R., Scalmani, G., Barone, V., Mennucci, B., Petersson, G. A., Nakatsuji, H., Caricato, M., Li, X., Hratchian, H. P., Izmaylov, A. F., Bloino, J., Zheng, G., Sonnenberg, J. L., Hada, M., Ehara, M.; Toyota, K., Fukuda, R., Hasegawa, J., Ishida, M., Nakajima, T., Honda, Y., Kitao, O., Nakai, H.; Vreven, T., Montgomery, Jr., J. A., Peralta, J. E., Ogliaro, F., Bearpark, M., Heyd, J. J., Brothers, E., Kudin, K. N., Staroverov, V. N., Kobayashi, R., Normand, J., Raghavachari, K., Rendell, A., Burant, J. C., Iyengar, S. S., Tomasi, J., Cossi, M., Rega, N., Millam, J. M., Klene, M., Knox, J. E., Cross, J. B., Bakken, V., Adamo, C., Jaramillo, J., Gomperts, R., Stratmann, R. E., Yazyev, O., Austin, A. J., Cammi, R., Pomelli, C., Ochterski, J. W., Martin, R. L., Morokuma, K., Zakrzewski, V. G., Voth, G. A., Salvador, P., Dannenberg, J. J., Dapprich, S., Daniels, A. D., Farkas, Ö., Foresman, J. B., Ortiz, J. V., Cioslowski, J., and Fox, D. J. (2009) Gaussian, Inc., Wallingford CT

42. Becke, A. D., (1993) J. Chem. Phys. 98, 5648-52.

43. Ali, E. Md., Sanyal, B. and Oppeneer, P. M. (2012) J. Phys. Chem. B 116, 5849

44. Maseras, F., and Morokuma, K. (1995) J. Comput. Chem. 16, 1170–1179

45. http://www.cp2k.org; last accessed: August 6, 2014

46. VandeVondele, J., Krack, M., Mohamed F., Parrinello, M., Chassaing, T., and Hutter, J. (2005) Comp. Phys. Comm. 167 (2), 103-128

47. VandeVondele, J., and Hutter, J. (2007) J. Chem. Phys. 127, 114105

48. Brooks, B.R., Brooks, C. L. 3rd, Mackerell, A. D. Jr, Nilsson, L., Petrella, R. J., Roux, B., Won, Y., Archontis, G., Bartels, C., Boresch, S., Caflisch, A., Caves, L., Cui, Q., Dinner, A. R., Feig, M., Fischer, S., Gao, J., Hodoscek, M., Im, W., Kuczera, K., Lazaridis, T., Ma, J., Ovchinnikov, V., Paci, E., Pastor, R. W., Post, C. B., Pu, J. Z., Schaefer, M., Tidor, B., Venable, R. M., Woodcock, H. L., Wu, X., Yang, W., York, D. M., and Karplus, M. (2009) Journal of Computational Chemistry 30 (10), 1545–1614

49. Laino, T., Mohamed, F., Laio, A., and Parrinello, M. (2005) J. Chem. Theory and Comp. 1 (6), 1176-1184

50. Maragliano, L., and Vanden-Eijnden E. (2008) J. Chem. Phys. 128, 184110

51. Marcus, R.A. (1956) J. Chem. Phys. 24, 966

52. Marcus, R.A. (1956) J. Chem. Phys. 24, 979